# Direct numerical simulation of turbulent slope flows up to Grashof number $Gr = 2.1 \times 10^{11}$

**M. G. Giometto**[1,†], **G. G. Katul**[2], **J. Fang**[3] **and M. B. Parlange**[1,‡]

[1]Department of Civil Engineering, University of British Columbia, Vancouver, BC V6T 1Z4, Canada

[2]Nicholas School of the Environment, Duke University, Durham, NC 27708, USA

[3]School of Architecture, Civil and Environmental Engineering, École Polytechnique Fédérale de Lausanne, Lausanne, VD 1015, Switzerland

Stably stratified turbulent flows over an unbounded, smooth, planar sloping surface at high Grashof numbers are examined using direct numerical simulations (DNS). Four sloping angles ($\alpha = 15°$, $30°$, $60°$ and $90°$) and three Grashof numbers ($Gr = 5 \times 10^{10}$, $1 \times 10^{11}$ and $2.1 \times 10^{11}$) are considered. Variations in mean flow, second-order statistics and budgets of mean- (MKE) and turbulent-kinetic energy (TKE) are evaluated as a function of $\alpha$ and $Gr$ at fixed molecular Prandtl number ($Pr = 1$). Dynamic and energy identities are highlighted, which diagnose the convergence of the averaging operation applied to the DNS results. Turbulent anabatic (upward moving warm fluid along the slope) and katabatic (downward moving cold fluid along the slope) regimes are identical for the vertical wall set-up (up to the sign of the along-slope velocity), but undergo a different transition in the mechanisms sustaining turbulence as the sloping angle decreases, resulting in stark differences at low $\alpha$. In addition, budget equations show how MKE is fed into the system through the imposed surface buoyancy, and turbulent fluctuations redistribute it from the low-level jet (LLJ) nose towards the boundary and outer flow regions. Analysis of the TKE budget equation suggests a subdivision of the boundary layer of anabatic and katabatic flows into four distinct thermodynamical regions: (i) an outer layer, corresponding approximately to the return flow region, where turbulent transport is the main source of TKE and balances dissipation; (ii) an intermediate layer, bounded below by the LLJ and capped above by the outer layer, where the sum of shear and buoyant production overcomes dissipation, and where turbulent and pressure transport terms are a sink of TKE; (iii) a buffer layer, located at $5 \lesssim z^+ \lesssim 30$, where TKE is provided by turbulent and pressure transport terms, to balance viscous diffusion and dissipation; and (iv) a laminar sublayer, corresponding to $z^+ \lesssim 5$, where the influence of viscosity is significant. $(\cdot)^+$ denotes a quantity rescaled in inner units. Interestingly, a zone of global backscatter (energy transfer from the turbulent eddies to the mean flow) is consistently found in a thin layer below the LLJ in both anabatic and katabatic regimes.

**Key words:** atmospheric flows, boundary layer structure, meteorology

† Email address for correspondence: mgiometto@civil.ubc.ca

‡ Department of Civil and Environmental Engineering, Monash University, Clayton, VIC 3800, Australia.

## 1. Introduction

When an inclined surface is thermally altered from the state of the overlying fluid, the resulting buoyancy force projects in both the along- and normal-to-slope directions. Surface cooling results in a downslope flow (katabatic flow), whereas surface heating generates an upslope flow (anabatic flow). The significance of such sloping turbulent flows is rarely questioned given their ubiquity and their central role in land–atmosphere exchange processes. Katabatic and anabatic flows are persistent over complex terrains (Whiteman 1990; Monti *et al.* 2002; Rampanelli, Zardi & Rotunno 2004; Haiden & Whiteman 2005; Rotach & Zardi 2007; Fernando 2010; Zardi & Whiteman 2013; Nadeau *et al.* 2013*a*; Oldroyd *et al.* 2014, 2016*b*; Fernando *et al.* 2015; Lehner *et al.* 2015; Grachev *et al.* 2016; Hang *et al.* 2016; Jensen *et al.* 2016), and despite their local nature, their interaction with larger-scale forcing mechanisms can favour the development of cyclonic vorticity in the middle and upper troposphere (Parish 1992; Parish & Bromwich 1998). Katabatic winds regulate energy, momentum and mass transfer over the ice sheets of Greenland and Antarctica (Egger 1985; Parish 1992; Parish & Bromwich 1998; Renfrew 2004; Renfrew & Anderson 2006), and also influence the movement of the marginal ice zone (Chu 1987). In addition, katabatic flows are a permanent feature of the atmospheric boundary layer (ABL) over melting glaciers (Greuell *et al.* 1994; Smeets, Duynkerke & Vugts 1997; Oerlemans 1998; Oerlemans *et al.* 1999; Smeets, Duynkerke & Vugts 2000; Parmhed, Oerlemans & Grisogono 2004), whose constant retreat is a matter of public interest, given their impact on both the sea level rise and on water resource management.

Prandtl (1942) framed the problem of slope flows in a conceptually simple model, considering a doubly infinite (no leading edges) plate that is uniformly heated or cooled and lies within a stably stratified environment. The Prandtl model (Prandtl 1942) states that the advection of base-state (environmental) potential temperature is balanced by buoyancy (diffusive) flux divergence, whereas the slope-parallel component of buoyancy balances momentum (diffusive) flux divergence. This particular type of flows are termed equilibrium flows (Mahrt 1982), given the nature of the balance between a turbulent flux divergence and a generation/destruction mechanism. Under such settings, the Boussinesq equations of motion and thermal energy reduce to one-dimensional form, which allows for analytical treatment. Accounting for a base stable stratification admits solutions that approach steady-state conditions at large times, whereas in the absence of a stable stratification (classical solutions), the thermal and dynamic boundary layers (TBL and DBL in the following) grow in an unbounded manner (Menold & Yang 1962).

The original model assumed constant turbulent diffusivities (labelled as K) – and is therefore incapable of representing the observed steep near-surface gradients (Grisogono & Oerlemans 2001*b*). In addition, the return flow region predicted by the constant-K solution is usually stronger, when compared to measurements or numerical simulations, and also vanishes more rapidly away from the surface (Defant 1949; Denby 1999; Grisogono & Oerlemans 2001*b*). This limitation was first overcome in Gutman (1983), where a patched analytic solution was proposed, valid for linearly decreasing K in the inner flow regions. More recently, Grisogono & Oerlemans (2001*b*, 2002) proposed an approximate analytical solution able to account for gradually varying eddy diffusivities, valid under the WKB approximation (after Wentzel–Kramers–Brillouin), and a closed form solution valid for O'Brien type K was derived in Giometto *et al.* (2017). Modifications of the Prandtl model to allow for

variations in surface forcing (Shapiro & Fedorovich 2007, 2008; Burkholder, Shapiro & Fedorovich 2009), to account for Coriolis effects (Kavavcic & Grisogono 2007; Shapiro & Fedorovich 2008), time dependence of the solution (Shapiro & Fedorovich 2004, 2005, 2008; Zardi & Serafin 2015) and for weakly nonlinear effects (Grisogono *et al.* 2014; Güttler *et al.* 2016), were also recently proposed.

The Prandtl conceptual approach is also of interest in numerical modelling. It alleviates computational costs by constraining the geometry to regular domains, thus allowing the use of efficient numerical schemes such as methods based on finite differences or spectral expansions. The existence of a statistically steady-state solution also provides a benchmark for quantitative analysis. The past decades have seen significant advances in computational performance, achieved through both improvements in computer hardware and in numerical algorithms that solve differential equations. Nevertheless, computational cost of simulating high Reynolds number (*Re*) flows over long slopes remains prohibitively high, and has motivated the use of closure models that aim at reducing resolution requirements in the dissipative range, especially when energy-containing scales are of primary interest (Pope 2000). Since the pioneering work of Schumann (1990), large-eddy simulation (LES) has represented one of the workhorses for the simulation of slope flows within the Prandtl model framework. It has revealed several aspects of the turbulent structure and illustrated the sensitivity of the bulk solution to the system parameters (Skyllingstad 2003; Axelsen & Dop 2009*a*,*b*; Grisogono & Axelsen 2012). LES of slope flows in more complex configurations (i.e. not relying on the Prandtl model set-up) have been performed in Smith & Skyllingstad (2005), where the effects of varying slope angle were analysed, and the interaction of slope flows with valley systems have also been recently addressed via LES (Chow *et al.* 2006; Weigel *et al.* 2006; Chemel, Staquet & Largeron 2009; Burns & Chemel 2014, 2015; Arduini, Staquet & Chemel 2016). However, the stable stratification and the peculiar features characterizing slope flows (e.g. the presence of zero-gradient layers in the state variables) question the validity of the assumptions upon which LES subgrid-scale (SGS) models are derived (Burkholder, Fedorovich & Shapiro 2011). In addition, the lack of a rigorous similarity theory for slope flows (Mahrt 1998; Grisogono & Oerlemans 2001*a*; Grisogono, Kraljevic & Jericevic 2007; Mahrt 2013; Nadeau *et al.* 2013*b*; Monti, Fernando & Princevac 2014; Oldroyd *et al.* 2016*a*) makes it impossible to prescribe adequate surface fluxes in simulations. These limitations have motivated the use of direct numerical simulations (DNS), which, despite their modest range of *Re*, provide the most comprehensive view of the flow structure (Fedorovich & Shapiro 2009) (FS09 hereafter). These studies showed that slope-flow statistics are sensitive to variations in the parameter space, including the magnitude of the surface forcing, the slope angle and the strength of the ambient stratification. They all play a role in determining the characteristics of the flow. This finding motivated recent efforts towards a derivation of scaling relations that allow the elimination of the dependency of the solution on the sloping angle (Shapiro & Fedorovich 2014). Scaling relations are of interest since they facilitate the design of experiments and have potentials to yield significant computational savings in parametric studies when explored through LES and DNS.

In this work, the problem of anabatic and katabatic flows and the properties of the LLJ in the near-wall region are explored using high resolution DNS. The focus is on variations in the slope-normal structure of selected flow statistics and in integrated quantities as a function of the sloping angle ($\alpha$) and of the Grashof number (*Gr*). The flow is driven by a homogeneous constant surface buoyancy force and the molecular Prandtl number (*Pr*) is set to unity (instead of a typical 0.7 value
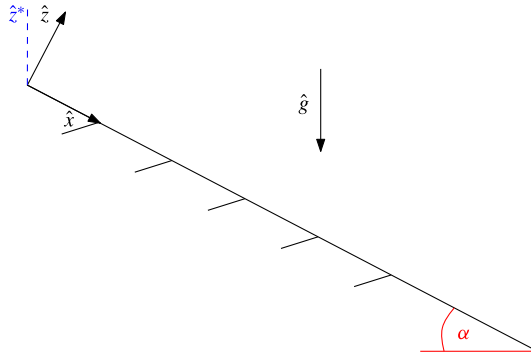
FIGURE 1. Slope-aligned coordinate system.

for air) in line with the FS09 study. The current study complements and extends the work of FS09, where a similar set-up was adopted to characterize slope flows driven by an imposed surface buoyancy flux. The aim is to shed additional light on the interactions between turbulence and the mean flow state as well as the role of the low-level jet (LLJ) in energy and momentum exchanges. Specifically, the study aims at (i) assessing how $\alpha$ and $Gr$ influence katabatic and anabatic flows when constant surface buoyancy is prescribed; (ii) contrasting key features between slope flows driven by a constant imposed surface buoyancy, when compared against slope flows generated by a constant imposed surface buoyancy flux; and (iii) characterizing the vertical structures (and their sensitivity to variations in the parameter space) of mean kinetic energy (MKE) and of turbulent kinetic energy (TKE) budget terms. The long-term goal is to provide improvements for current turbulence closure models for sloping and stable conditions that can then be implemented in large-scale atmospheric models so as to address the plethora of problems already highlighted earlier on in the introduction. The manuscript is organized as follows. The governing equations for the problem are derived in §2. Section 3 provides details on the numerical algorithm and on the set-up of simulations and the main results are presented in §4. Summary and concluding remarks follow in §5.

## 2. Equations of motion

Thermal convection of turbulent stratified fluid flow over sloping surfaces can be described in a slope-rotated reference system, where $\hat{x}$ is the along-slope direction, $\hat{y}$ denotes the spanwise direction and $\hat{z}$ is the slope-normal direction, as displayed in figure 1. $(\hat{\cdot})$ indicates a dimensional variable. The potential temperature $\hat{\theta}(\hat{x}, \hat{t})$ is decomposed into a base state $\hat{\theta}^R(\hat{z}^*)$ and a perturbation component $\hat{\theta}''(\hat{x}, \hat{t}) \equiv \hat{\theta}(\hat{x}, \hat{t}) - \hat{\theta}^R(\hat{z}^*)$ as originally proposed by Prandtl (1942). Assuming the base state $\hat{\theta}^R(\hat{z}^*)$ to be a linear function of the vertical coordinate direction $\hat{z}^*$, results in $\hat{N} \equiv \sqrt{\hat{\beta}(\mathrm{d}\hat{\theta}^R/\mathrm{d}\hat{z}^*)} = \mathrm{const.}$, where $\hat{N}$ is the buoyancy frequency (equivalent to the Brunt–Väisälä frequency). The thermal expansion coefficient $\hat{\beta} \equiv \hat{g}/\hat{\theta}_0$ where $\hat{g}$ is the acceleration due to gravity and $\hat{\theta}_0$ is a reference constant temperature. Moreover, invoking the Boussinesq approximation (i.e. ignoring density differences except where they appear in terms multiplied by $\hat{g}$) and neglecting earth rotation effects, the

conservation equations within the DBL and TBL in dimensional form reduce to

$$\frac{\partial \hat{u}_i}{\partial \hat{t}} + \frac{\partial \hat{u}_i \hat{u}_j}{\partial \hat{x}_j} = -\frac{\partial \hat{\pi}}{\partial \hat{x}_i} + \hat{\nu} \frac{\partial^2 \hat{u}_i}{\partial \hat{x}_j^2} - \hat{\beta} \hat{\theta}''(\hat{\boldsymbol{x}}, \hat{t})[\delta_{i1} \sin \alpha - \delta_{i3} \cos \alpha], \quad (2.1)$$

$$\frac{\partial \hat{u}_i}{\partial \hat{x}_i} = 0, \quad (2.2)$$

$$\frac{\partial \hat{\theta}''}{\partial \hat{t}} + \frac{\partial \hat{u}_j \hat{\theta}''}{\partial \hat{x}_j} = -\frac{\partial \hat{u}_j \hat{\theta}^R}{\partial \hat{x}_j} + \hat{\kappa} \frac{\partial^2 \hat{\theta}''}{\partial \hat{x}_j^2}, \quad (2.3)$$

where $\hat{t}$ (s) denotes time, $\hat{u}_i$ (m s$^{-1}$), $i = 1, 2, 3$, are the velocity components in the three coordinate directions $(\hat{x}, \hat{y}, \hat{z})$ (m), $\hat{\pi} \equiv [\hat{p} - \hat{p}^R(\hat{x}, \hat{z})]/\hat{\rho}_0$ (m$^2$ s$^{-2}$) is the normalized deviation of kinematic pressure from the background hydrostatic state, $\hat{\rho}_0$ (kg m$^{-3}$) is a reference constant density, $\alpha$ (rad) is the slope angle, $\hat{\nu}$ (m$^2$ s$^{-1}$) and $\hat{\kappa}$ (m$^2$ s$^{-1}$) are the kinematic molecular viscosity and thermal diffusivity coefficients, and $\delta_{ij}$ is the Kronecker Delta function. Molecular dissipation of kinetic energy represents an additional source of heat, and should in principle be included in the equation for $\hat{\theta}$. However, due to the low velocities involved in slope flows this term is small and has thus been neglected. Introducing the buoyancy variable $\hat{b}(\hat{\boldsymbol{x}}, \hat{t}) \equiv \hat{\beta} \hat{\theta}''(\hat{\boldsymbol{x}}, \hat{t})$, and since $\hat{z}^*(\hat{\boldsymbol{x}}) \equiv -\hat{x} \sin \alpha + \hat{z} \cos \alpha$, equations (2.1)–(2.3) can be re-written as in FS09

$$\frac{\partial \hat{u}_i}{\partial \hat{t}} + \frac{\partial \hat{u}_i \hat{u}_j}{\partial \hat{x}_j} = -\frac{\partial \hat{\pi}}{\partial \hat{x}_i} + \hat{\nu} \frac{\partial^2 \hat{u}_i}{\partial \hat{x}_j^2} - \hat{b}(\hat{\boldsymbol{x}}, \hat{t})[\delta_{i1} \sin \alpha - \delta_{i3} \cos \alpha], \quad (2.4)$$

$$\frac{\partial \hat{u}_i}{\partial \hat{x}_i} = 0, \quad (2.5)$$

$$\frac{\partial \hat{b}}{\partial \hat{t}} + \frac{\partial \hat{u}_j \hat{b}}{\partial \hat{x}_j} = \hat{N}^2 [\hat{u}_1 \sin \alpha - \hat{u}_3 \cos \alpha] + \hat{\kappa} \frac{\partial^2 \hat{b}}{\partial \hat{x}_j^2}. \quad (2.6)$$

## 2.1. *Normalization of the equations and governing parameters*

To express the governing equations as a function of suitable dimensionless parameters, a characteristic time, length, buoyancy and velocity scale can be defined as

$$\hat{T} \equiv \hat{N}^{-1}, \quad \hat{L} \equiv \frac{|\hat{b}_s|}{\hat{N}^2}, \quad \hat{B} \equiv |\hat{b}_s|, \quad \hat{U} \equiv \frac{|\hat{b}_s|}{\hat{N}}, \quad (2.7a{-}d)$$

where the surface buoyancy $\hat{b}_s$ determines whether the flow is anabatic ($\hat{b}_s > 0$) or katabatic ($\hat{b}_s < 0$). These aforementioned parameters can now be used to introduce the following normalized variables

$$t \equiv \hat{t}/\hat{T}, \quad x_i \equiv \hat{x}_i/\hat{L}, \quad b \equiv \hat{b}/\hat{B}, \quad u_i \equiv \hat{u}_i/\hat{U}, \quad \pi \equiv \hat{\pi}/\hat{U}^2. \quad (2.8a{-}e)$$

Relations (2.7) are derived selecting $\hat{b}_s$ and $\hat{N}$ as repeating parameters though this choice is by no means unique and other options are possible. Substituting the expressions (2.8) into the governing equations (2.4)–(2.6) results in

$$\frac{\partial u_i}{\partial t} + \frac{\partial u_i u_j}{\partial x_j} = -\frac{\partial \pi}{\partial x_i} - b(\delta_{i1} \sin \alpha - \delta_{i3} \cos \alpha) + Gr^{-1/2} \frac{\partial^2 u_i}{\partial x_j^2}, \quad (2.9)$$

| Label | $L_x \times L_y \times H$ | $N_x \times N_y \times N_z$ | $\alpha$ (deg.) | $T$ | $Gr$ | $b_s$ |
|---|---|---|---|---|---|---|
| U90H, S90H | $0.241^2 \times 0.324$ | $384^2 \times 1032$ | 90 | 6.28 | $2.1 \times 10^{11}$ | $\pm 1$ |
| U60H, S60H | $0.241^2 \times 0.324$ | $384^2 \times 1032$ | 60 | 7.25 | $2.1 \times 10^{11}$ | $\pm 1$ |
| U30H, S30H | $0.241^2 \times 0.324$ | $384^2 \times 1032$ | 30 | 12.57 | $2.1 \times 10^{11}$ | $\pm 1$ |
| U15H, S15H | $0.241^2 \times 0.324$ | $384^2 \times 1032$ | 15 | 24.28 | $2.1 \times 10^{11}$ | $\pm 1$ |
| U60M, S60M | $0.241^2 \times 0.324$ | $256^2 \times 1032$ | 60 | 7.25 | $1.0 \times 10^{11}$ | $\pm 1$ |
| U60L, S60L | $0.241^2 \times 0.324$ | $256^2 \times 1032$ | 60 | 7.25 | $5.0 \times 10^{10}$ | $\pm 1$ |

TABLE 1. Geometry and parameters for the DNS runs. $L_i$ and $N_i$ denote the domain size and the number of collocation nodes in the three coordinate directions, respectively, $T$ denotes the characteristic oscillation period characterizing the buoyancy and velocity fields (see § 3.4), $Gr \equiv \hat{b}_s^4 \, \hat{v}^{-2} \, \hat{N}^{-6}$ where $b_s$ is the imposed (normalized) surface buoyancy. Simulation labels indicate whether a specific run is in buoyantly [U]nstable or [S]table regime ($b_s = +1$ and $b_s = -1$ respectively), the surface sloping angles $\alpha$, and which among the three considered Grashof numbers ([H]igh, [M]edium and [L]ow) is used; for instance U30H denotes an anabatic flows regime with $\alpha = 30°$ at the highest among the considered Grashof numbers.

$$\frac{\partial u_i}{\partial x_i} = 0, \qquad (2.10)$$

$$\frac{\partial b}{\partial t} + \frac{\partial u_j b}{\partial x_j} = (u_1 \sin \alpha - u_3 \cos \alpha) + (Gr^{-1/2} Pr^{-1})\frac{\partial^2 b}{\partial x_j^2}, \qquad (2.11)$$

where $Gr \equiv \hat{b}_s^4 \, \hat{v}^{-2} \, \hat{N}^{-6}$ is the Grashof number, defined as the ratio between buoyancy and viscous forces. There are a number of advantages to adopting $Gr$ over other possible dimensionless numbers (e.g. Reynolds number). For the particulars of sloping flow with zero slip at the boundary, $Gr$ measures the relative strength of the body (or non-contact) force to the surface (or contact) force arising from friction (or viscosity). The flow adjustment to this imbalance gives rise to non-hydrostatic pressure distribution and advective acceleration.

## 3. Simulations

Equations (2.9)–(2.11) are integrated across a range of sloping angles, $\alpha$ and $Gr$ numbers, considering both anabatic (upslope) and katabatic (downslope) flow regimes, as summarized in table 1. Given the computational cost of DNS, variations in $Gr$ are limited to the $\alpha = 60°$ case.

Note that $(b, \alpha) \rightarrow (-b, \alpha + \pi)$ is a symmetry transformation for the system (2.9)–(2.11), and therefore cases U90H and S90H are equivalent up to a change in the sign of $u_i$. Because of this symmetry, a heated wall at $\alpha = 15°$ is equivalent to a cooled wall at $\alpha = 15° + 180°$.

The DNS algorithm is a modification of the code previously used to study land–atmosphere interaction processes (Albertson & Parlange 1999*a,b*; Kumar *et al.* 2006; Bou-Zeid *et al.* 2009; Calaf, Meneveau & Meyers 2010; Calaf, Parlange & Meneveau 2011; Giometto *et al.* 2016; Sharma *et al.* 2016; Sharma, Parlange & Calaf 2017), to develop and test linear and nonlinear LES subgrid-scale models (Porté-Agel, Meneveau & Parlange 2000; Higgins, Parlange & Meneveau 2003; Bou-Zeid, Meneveau & Parlange 2005; Lu & Porté-Agel 2010; Abkar, Bae & Moin 2016), to design surface-flux parameterizations (Hultmark, Calaf & Parlange 2013)

and to model scalar transport processes (Chamecki, Meneveau & Parlange 2009). Equations are solved in rotational form to ensure conservation of mass and kinetic energy (Orszag & Pao 1975). A pseudospectral collocation approach (Orszag 1969, 1970) based on truncated Fourier expansions is used in the $x, y$ coordinate directions whereas a second-order accurate centred finite differences scheme is adopted in the slope-normal direction, requiring a staggered grid approach for the $u$, $v$, $p$, $b$ state variables (these are stored at $(i + 1/2)\Delta_Z$, where $i$ denotes a given layer of collocation nodes in the slope-normal direction). Time integration is performed adopting a fully explicit second-order accurate Adams–Bashforth scheme. A fractional step method (Chorin 1968; Temam 1968) is adopted to compute the pressure field by solving an additional Poisson equation, which is derived enforcing mass continuity for the incompressible fluid ($\partial u_i/\partial x_i = 0$). Further, all nonlinear terms are fully de-aliased adopting a 3/2 rule so as to avoid artificial pile up of energy at the high wavenumber range (Kravchenko & Moin 1997; Canuto *et al.* 2006).

Equations are integrated over a regular domain $[0, L_x] \times [0, L_y] \times [0, H]$, with boundary conditions $u_i(x, y, 0) = u_i(x, y, H) = b(x, y, H) = 0$ and $b(x, y, 0) = \hat{b}_s/\hat{B} = \pm 1$.

A sponge layer (Israeli & Orszag 1981) is applied to the top 20 % of the computational domain so as to damp spurious internal wave reflections. The thickness of the sponge layer has been chosen based on a sensitivity analysis performed on the S15H case, which showed that a minimum of 15 % thickness is required to avoid non-negligible TKE at the top of the computational domain.

To guide the choice of the grid stencil an estimate of $\eta_\star = Gr^{-3/8}\tau_{bz}^{-1/4}$ for the $\alpha = 90°$ case was first evaluated from the Prandtl laminar flow analytic solution, where $\eta_\star$ is an equivalent of the Kolmogorov scale (FS2009) in the chosen normalized units, and where $\tau_{bz}$ denotes the normalized kinematic surface buoyancy flux. Subsequently the grid stencils were set to $\Delta_x = \Delta_y = 2\Delta_z = 2\eta_\star$. The resolvability condition $\Delta < 2\eta$ (Pope 2000) has been checked *a posteriori* (not shown) for all the considered cases, where $\eta = Gr^{-3/8}\epsilon^{-1/4}$ is the Kolmogorov length scale in normalized units. The vertical grid stencil satisfies such a criterion in all cases, whereas the horizontal grid stencil is often off by a factor of two, hence the need to verify the quality of proposed results. To do so, a higher resolution DNS katabatic run was performed at a sloping angle $\alpha = 90°$, halving the horizontal grid stencil (i.e. doubling the resolution in the horizontal directions). Note that the Kolmogorov scale is usually larger in stable cases than in the neutral ones, hence slope flows over vertical walls ($\alpha = 90°$) have the most stringent resolution requirements. First- and second-order statistics are found to be in good agreement with those presented herein, supporting the working conjecture that the current resolution is sufficient to represent most of the dissipative scales. The resulting domain size (see table 1) allows the representation of coherent structures populating the DBL and TBL at all the considered sloping angles (a domain-size convergence study was performed for the anabatic case at $\alpha = 15°$ to support such assertion, and variations of statistics were found to be negligible).

Simulations are run for a minimum of $6T$, where $T = 2\pi \sin^{-1}\alpha$ is the characteristic (normalized) period of internal waves that arise in the system due to the imposed stable background stratification. Statistics are computed over the last $5T$ for the cases $\alpha = 90°$, $\alpha = 60°$, and over the last $3T$ for the cases $\alpha = 30°$, $\alpha = 15°$ (previous time steps are disregarded to allow turbulence to fully develop). All simulations are performed using $Pr = 1$, in line with previous studies of slope flows (FS09). Throughout, $\langle \cdot \rangle$ denotes averaging in time and along spatial coordinates of statistical homogeneity $(x, y)$ and fluctuations with respect to time and space averages ($\langle \cdot \rangle$) are expressed as $(\cdot)'$.
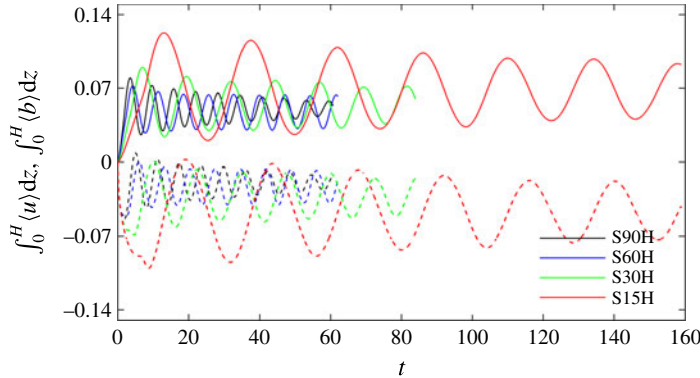
FIGURE 2. Time evolution of slope-normal integrated $\langle u \rangle$ (solid lines) and $\langle b \rangle$ (dashed lines) fields for simulations S90H, S60H, S30H and S15H (katabatic flow regime). The total time integration period is shown for each run.

## 4. Results and discussion

Throughout this section, unless otherwise stated, all results and comments regard cases characterized by $Gr = 2 \times 10^{11}$. Variations of the solution with respect to $Gr$ are described and commented in appendix A.

### 4.1. *Time evolution and structure of the flow*

The time evolution of the slope-normal integrated, space-averaged ($x$, $y$ directions), normalized streamwise velocity $\langle u \rangle$ and buoyancy $\langle b \rangle$ is displayed in figure 2. The system exhibits the classical quasi-periodic, low-frequency, oscillatory behaviour (surges), superimposed to a base flow, as observed in FS09 and in experiments (e.g. Doran & Horst 1981; Monti *et al.* 2002; Princevac, Hunt & Fernando 2008). It can be shown (McNider 1982) that the slope-normal integrated $\langle u \rangle$, $\langle b \rangle$ variables resemble a system of coupled oscillators, which in the case of laminar flow are characterized by a period $\hat{T} \approx 2\pi(\hat{N} \sin \alpha)^{-1}$ (normalized period is $T \approx 2\pi/\sin \alpha$). The oscillation periods from DNS are very close to those of corresponding laminar solutions, which for typical atmospheric values $\hat{N} = 10^{-2}$ (Hz), $\alpha = 15°$, $30°$ and $60°$, are 40, 20 and 10 min. A recent study (Fedorovich & Shapiro 2017) has shown how damping of integral oscillations by surface stress in laminar Prandtl flows decays very rapidly and independently from the flow forcing mechanism. Such fast reduction in the damping factor was also observed in the turbulent slope flows simulated in FS09. Current results further support such findings, i.e. observed integral oscillations are characterized by a progressively weaker decay rate as time advances.

Averaging equations (2.9)–(2.11) in time and over directions of statistical homogeneity ($x$, $y$) results in

$$\langle b \rangle \sin (\alpha) = \frac{\mathrm{d}\langle \tau_{xz}^{tot} \rangle}{\mathrm{d}z}, \tag{4.1}$$

$$\langle u \rangle \sin (\alpha) = -\frac{\mathrm{d}\langle \tau_{bz}^{tot} \rangle}{\mathrm{d}z}, \tag{4.2}$$

where $\langle \tau_{xz}^{tot} \rangle = Gr^{-1/2}(\mathrm{d}\langle u \rangle/\mathrm{d}z) - \langle u'w' \rangle$ and $\langle \tau_{bz}^{tot} \rangle = Gr^{-1/2}Pr^{-1}(\mathrm{d}\langle b \rangle/\mathrm{d}z) - \langle b'w' \rangle$ are the normalized total (molecular + turbulent) slope-normal kinematic momentum
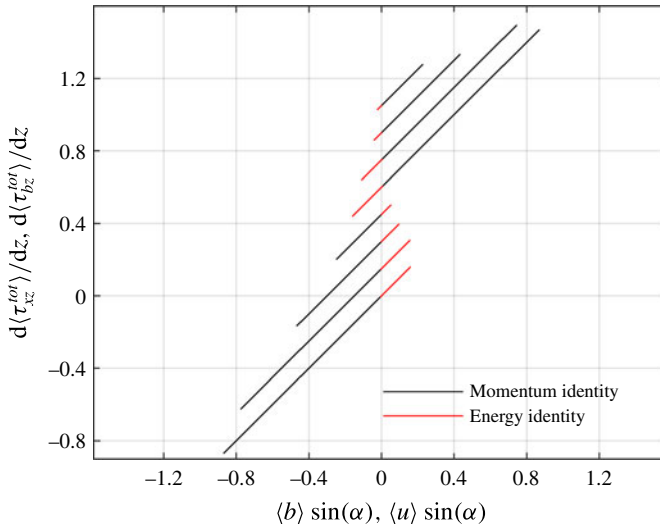
FIGURE 3. Dynamic (black lines) and energy (red lines) identities (4.1) and (4.2) for the considered simulations. Profiles have been shifted on the $y$ axis to allow for proper visualization. From top to bottom, profiles correspond to U15H, U30H, U60H, U90H and S15H, S30H, S60H, S90H, respectively. We here denote $\langle \tau_{xz}^{tot} \rangle = Gr^{-1/2}(\mathrm{d}\langle u \rangle / \mathrm{d}z) - \langle u'w' \rangle$ and $\langle \tau_{bz}^{tot} \rangle = Gr^{-1/2}Pr^{-1}(\mathrm{d}\langle b \rangle / \mathrm{d}z) - \langle b'w' \rangle$ (sum of molecular and turbulent kinematic fluxes of streamwise momentum and buoyancy in the slope-normal direction).

and buoyancy fluxes. Equations (4.1) and (4.2) can be used to test the 'quality' of computed statistics (steady state is guaranteed only if the two identities hold). Numerical results are displayed in figure 3, and certify that averaging over $3T$, after a transient of at least $3T$ is sufficient to satisfy both equations (4.1) and (4.2).

Figures 4 and 5 display a pseudocolour plot of instantaneous streamwise normalized velocity field ($u$) and normalized buoyancy field ($b$) for simulations S60H, S15H and U60H, U15H, respectively. The TBL appears shallower than the DBL, as previously noted in FS09. A reversed flow characterizes the above-jet regions, resulting from the interaction between the flow and the background stably stratified environment, in qualitative agreement with the predictions of the Prandtl model (Prandtl 1942). Progressive dissimilarity in DBL and TBL boundary layer thickness arises as the sloping angle decreases from the reference $\alpha = 90°$ vertical wall set-up (recall that at $\alpha = 90°$ the two flow regimes are equal up to a sign in $u_i$). As $\alpha$ decreases, the LLJ regions in the anabatic flow solution experience a significant thickening induced by the convective type regime characterizing the flow at small sloping angles. Katabatic flows are instead characterized by a strong static stability at small sloping angles (see figure 4), which damps positive slope-normal velocity fluctuations, thus maintaining the LLJ relatively close to the wall and reducing the overall mixing of momentum and buoyancy in the near-wall regions. In addition, the strong stability induced by the imposed surface buoyancy in the katabatic flow regime at small $\alpha$ results in partial laminarization of the LLJ.

### 4.2. *Mean flow*

Mean profiles of kinematic momentum $\langle u \rangle$ and buoyancy $\langle b \rangle$ are displayed in figure 6. Computed quantities qualitatively resemble those from the classic constant-K Prandtl
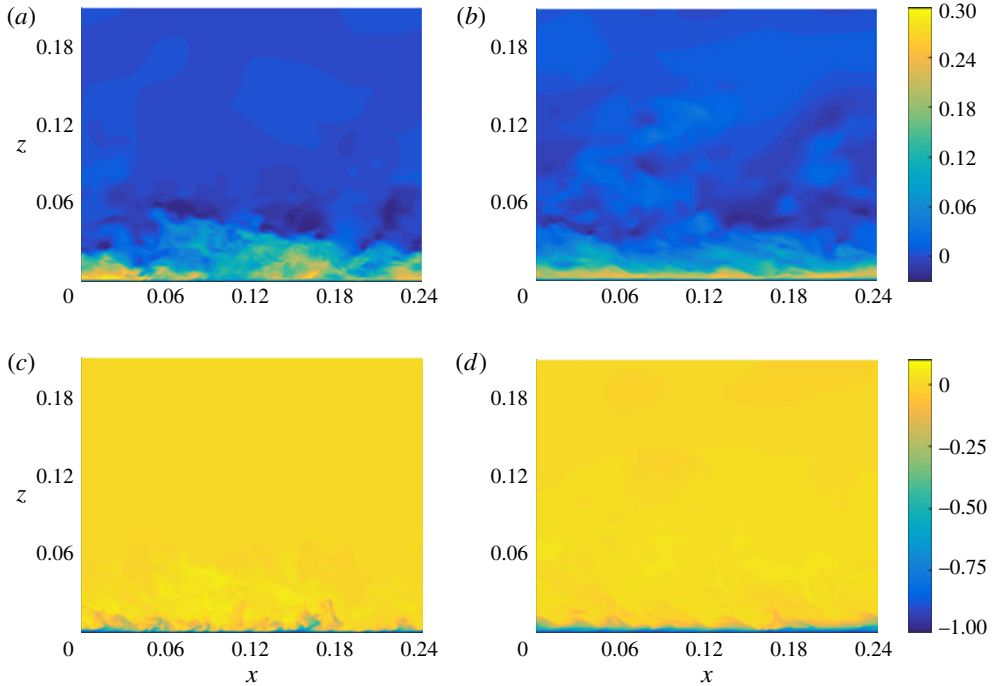
FIGURE 4. Pseudocolour plot of instantaneous katabatic flow streamwise velocity $u$ ($a,b$) and buoyancy $b$ ($c,d$), on the plane $y = L_y/2$ for simulations s60h ($a,c$) and s15h ($b,d$). The $z$-axis denotes the slope-normal coordinate direction, whereas the $x$-axis denotes the along-slope direction. The displayed $u(x, z)$ and $b(x, z)$ fields correspond to the crest of the last simulated oscillation for both runs. For detailed viewing, only the near-surface region of the total domain is shown.

analytic solution (Prandtl 1942). The most significant features are a peak velocity ($u_j$), the nose of the LLJ (occurring at $z_j$), and a return flow region capping both the DBL and TBL. As previously observed in FS09, such features are sensitive to the sloping angle ($\alpha$), and as $\alpha$ decreases from the vertical wall set-up ($\alpha = 90°$), the anabatic and katabatic flow solutions progressively depart from each other.

The constant-K Prandtl solution provides a useful framework for the interpretation of results, and is thus here briefly summarized. Based on the proposed normalization (see Sect. 2.1), the Prandtl one-dimensional solution for imposed constant surface buoyancy reads (FS09)

$$u = -b_s Pr^{-1/2} \sin(\sigma z) \exp(-\sigma z), \quad z \in [0, \infty), \tag{4.3}$$

$$b = b_s \cos(\sigma z) \exp(-\sigma z), \quad z \in [0, \infty), \tag{4.4}$$

where $\sigma = (Gr\, Pr^{-1})^{1/4} \sin(\alpha)^{1/2}$ and $b_s = \pm 1$. Note that (4.3) and (4.4) correspond to a laminar flow solution of the time and space averaged (2.9)–(2.11). It predicts a velocity maximum $u_j = \pm 1/\sqrt{2} \exp(-\pi/4)$ that is independent of the sloping angle ($\alpha$), whereas the characteristic length scale of the flow $L \propto \sin(\alpha)^{-1/2}$ whereby $z_j \propto \sin(\alpha)^{-1/2}$ (Grisogono & Axelsen 2012; Grisogono *et al.* 2014).
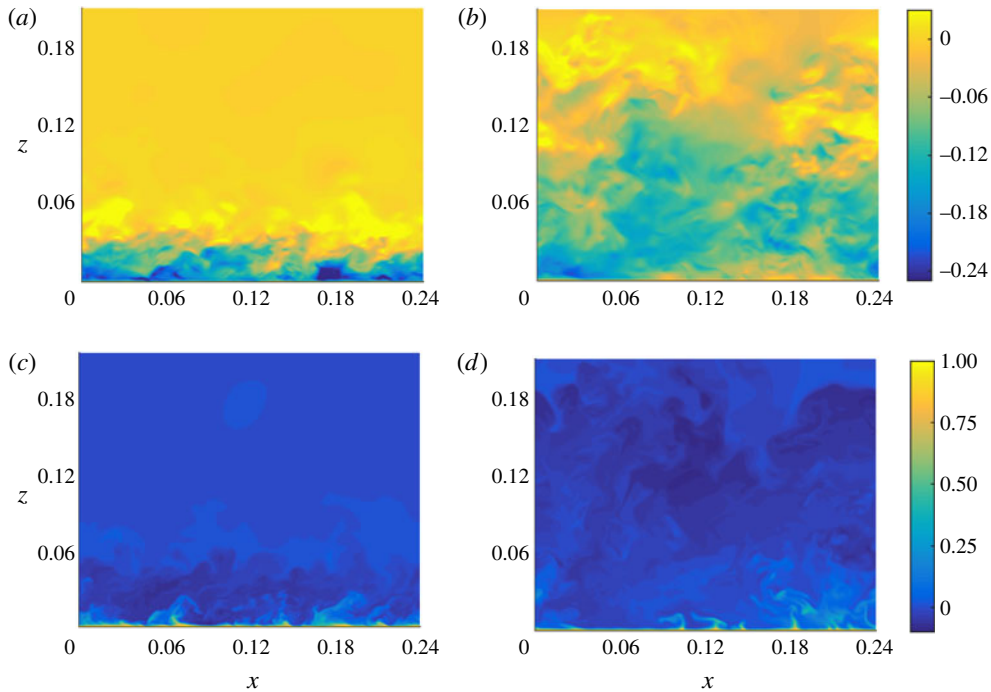
FIGURE 5. Pseudocolour plot of instantaneous anabatic flow streamwise velocity $u$ $(a,b)$ and buoyancy $b$ $(c,d)$, on the plane $y = L_y/2$ for simulations U60H $(a,c)$ and U15H $(b,d)$. The displayed $u(x,z)$ and $b(x,z)$ fields correspond to the crest of the last simulated oscillation for both runs. For detailed viewing, only the near-surface region of the total domain is shown.

The location of the LLJ for the katabatic flow DNS solution is in good agreement with prediction from the Prandtl laminar flow solution, i.e.

$$z_j \approx \frac{\pi}{4\sigma}. \tag{4.5}$$

Conversely, $u_j$ is significantly smaller (a reduction from $\approx 30\,\%$ to $\approx 50\,\%$ depending on the slope angle) when compared to the laminar solution, mainly due to additional diffusion of momentum caused by turbulent motions at $z_j$ (as shown in §4.5). In addition, $u_j$ is not independent of $\alpha$ as in the Prandtl model, but is characterized by a modest increase as $\alpha$ decreases. This behaviour can be explained by considering that as the sloping angle decreases, the stable stratification induced by the imposed surface buoyancy damps turbulent motions in the LLJ region, thus reducing turbulent mixing of momentum and resulting in a higher peak velocity $u_j$.

The anabatic flow solution is more sensitive to variations in the sloping angle, when compared to its katabatic counterpart. As $\alpha$ is reduced, a simultaneous increase in the height of the LLJ and a reduction in its peak speed are observed. Variations are significant when compared to those characterizing the katabatic solution and the laminar case. This pattern is related to the strengthening of the slope-normal component of the buoyancy force as $\alpha$ decreases ($b\delta_{i3}\cos\alpha$ in (2.9)). This results in an unstable near-wall stratification, which enhances the slope-normal flux of
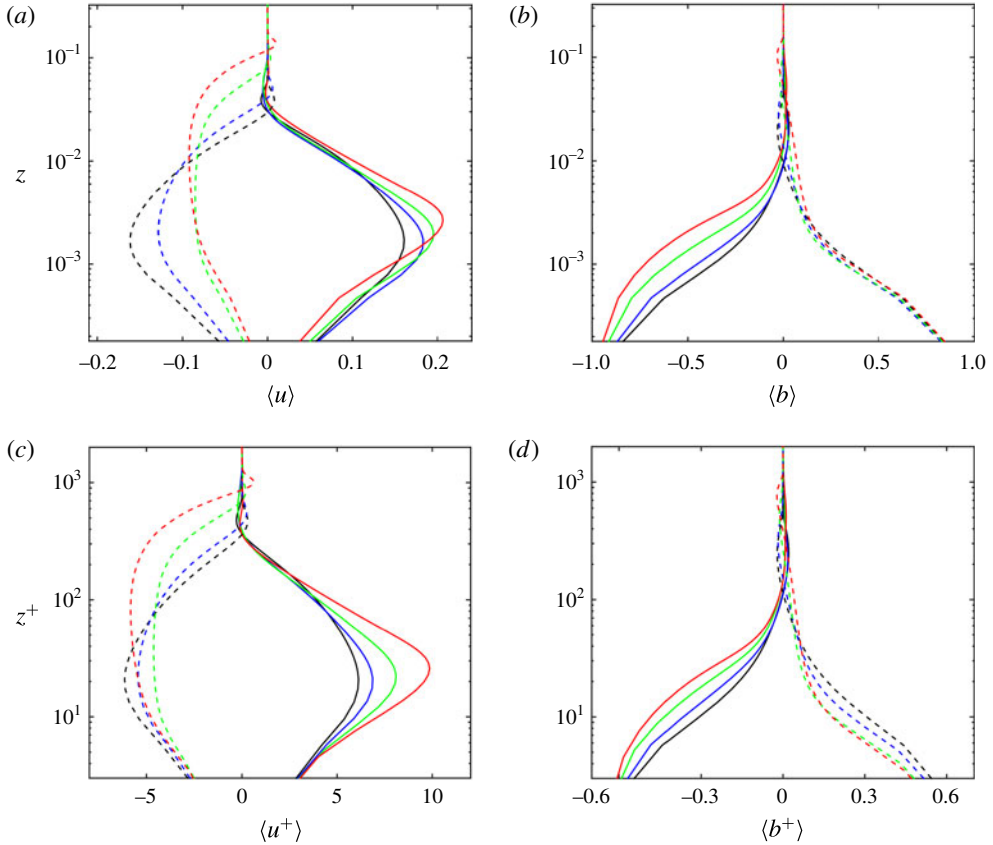
FIGURE 6. Comparison of streamwise mean velocity $\langle u \rangle$ (a) and $\langle u^+ \rangle$ (c) and of mean buoyancy $\langle b \rangle$ (b) and $\langle b^+ \rangle$ (d) for anabatic (dashed lines) and katabatic (solid lines) flows. Symbols: $\alpha = 90°$, black lines; $\alpha = 60°$, blue lines; $\alpha = 30°$, green lines; $\alpha = 15°$, red lines. All cases are characterized by $Gr = 2.1 \times 10^{11}$. The z-axis denotes the slope-normal coordinate direction.

momentum, and leads to progressively more mixed profiles of velocity and buoyancy in the LLJ regions, in agreement with the findings of FS09.

Figure 6 also features mean velocity and buoyancy profiles scaled with inner units, i.e. $z^+ = \hat{z} \hat{u}_\star / \hat{v}$, $u^+ = \hat{u}/\hat{u}_\star$, $b^+ = \hat{b}/\hat{b}_\star$ (where $\hat{u}_\star \equiv \sqrt{\langle \tau_{xz}^{tot} \rangle |_{z=0}}$ and $\hat{b}_\star \equiv (\langle \tau_{bz}^{tot} \rangle |_{z=0})/u_\star$, with $\tau_{xz}^{tot}$ and $\tau_{bz}^{tot}$ being the total kinematic momentum and buoyancy fluxes). The nose of the LLJ is located at $z^+ \approx 25$ in katabatic flows, separating the viscosity dominated wall regions from the turbulent outer layers. Anabatic flow solutions are characterized by a progressively more mixed LLJ as the sloping angle decreases, with peak speed at $z^+ \approx 100$ for $\alpha = 15°$, again highlighting a broadening of the DBL as the slope is reduced.

Another notable difference between the katabatic and the anabatic flow solutions is the sensitivity of the DBL and TBL thickness to $\alpha$. The DBL and TBL thickness ($\delta_d$ and $\delta_t$ respectively), which can be identified as the first and second zero crossing of $\langle b \rangle$ and $\langle u \rangle$ respectively are insensitive to $\alpha$ for the katabatic flow regime, whereas they vary by a factor of three across the considered $\alpha$-range for the anabatic flow solution. In line with this finding, the slope-normal integrated horizontal momentum
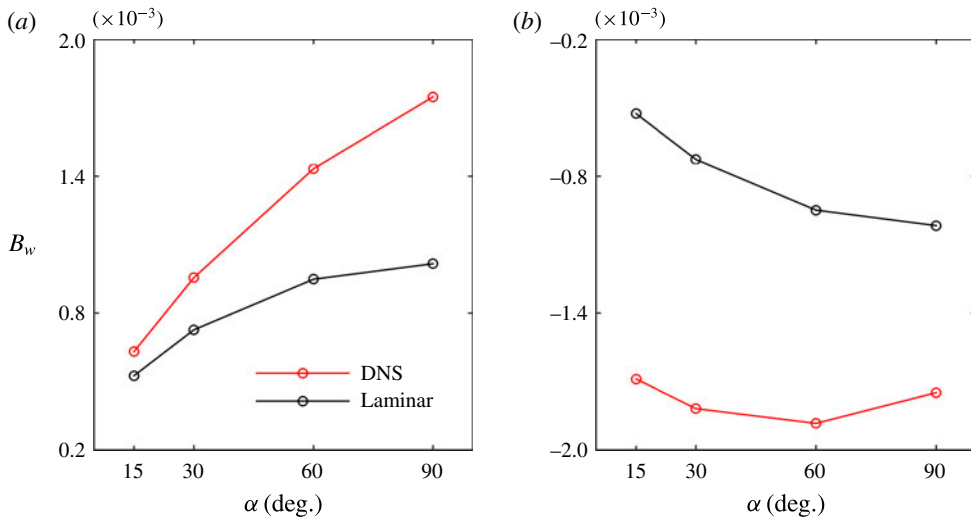
FIGURE 7. $\alpha$ dependence of the surface buoyancy flux $B_w$ for katabatic (*a*) and anabatic (*b*) flow cases. Simulations correspond to cases S90H, S60H, S30H, S15H and U90H, U60H, U30H, U15H for the katabatic and anabatic regimes, respectively. Predictions from the Prandtl laminar solution are included for comparison (black lines).

flux ($I_u$) in the anabatic flow regime is also strongly sensitive to variations in $\alpha$, whereas it is insensitive in the katabatic cases.

Such behaviour can be understood by integrating (4.2),

$$\int_0^H \langle u \rangle \, \mathrm{d}z = I_u = -\frac{B_w}{\sin \alpha}, \qquad (4.6)$$

where $B_w$ is the surface buoyancy flux. From (4.6) is apparent how larger $B_w$ and shallower slopes are characterized by larger $I_u$. Variations of the surface buoyancy flux as a function of $\alpha$ for the considered anabatic and katabatic cases are displayed in figure 7. As apparent, the anabatic flow solution is characterized by modest variations in $B_w$ across the considered $\alpha$ range, when compared against the katabatic flow cases. The latter experience a significant decrease in the surface buoyancy flux as the sloping angle decreases from $90°$ to $15°$, slowly approaching the surface flux predicted by the laminar flow solution (at $\alpha = 15°$ the difference between the DNS surface flux and the laminar solution surface flux is only 20 % the magnitude of the DNS surface flux itself). Such a behaviour is closely related to the strengthening of the near-surface inversion layer, which damps turbulent motions and leads to an apparent laminarization of the flow. In contrast, anabatic flows depart from the laminar solution as $\alpha$ decreases, due to the unstable stratification and likely onset of convective motions. Based on results shown in figure 7 one could introduce the equally crude approximations

$$B_w(\alpha)/B_w^{\alpha=90°} \approx 1 \quad \text{for anabatic flows}, \qquad (4.7)$$

$$B_w(\alpha)/B_w^{\alpha=90°} \approx \sin \alpha \quad \text{for katabatic flows}, \qquad (4.8)$$

which justifies the observed variations in the vertically integrated horizontal momentum flux in the anabatic and katabatic flow regimes based on (4.6).

Note that since $I_u = \mathcal{U}\mathcal{L}$, where $\mathcal{U}$ and $\mathcal{L}$ are the characteristic (normalized) velocity and length scale of the flow, and given that $\mathcal{U} \approx const.$ for both anabatic and katabatic flows, from (4.7) and (4.8) follows that $\mathcal{L} \propto 1/\sin\alpha$ for anabatic flows, and $\mathcal{L} \approx const.$ for katabatic flows. Such information can be of use for scaling purposes.

Given the strong $\alpha$ dependence of $B_w$ in the katabatic flow solution, profiles are expected vary significantly – when compared to those proposed herein – if a constant $B_w$ is used to drive the flow. Conversely, $B_w$ in the anabatic flow solution is weakly dependent on $\alpha$, and profiles are therefore expected to be poorly sensitive on the specific flow driving mechanisms (i.e. constant surface buoyancy or constant surface buoyancy flux). Because of this, the proposed anabatic flow solutions share strong similarities with those reported in the FS09 study, especially when considering the $\alpha$ dependence of $z_j$, $u_j$ and $\delta_d$, $\delta_t$, whereas the katabatic flow solutions differ significantly.

When a constant surface buoyancy flux is applied, the laminar flow solution is characterized by $z_j = \pi/(4\sigma)$ and $u_j \propto (\sin(\alpha))^{-1/2}$ (Grisogono & Axelsen 2012; Grisogono *et al.* 2014). Hence, $u_j$ increases as the sloping angle decreases and is not $\alpha$ independent as predicted by (4.3) and (4.4).

Similar variations in $z_j$ and a stronger $\alpha$ dependency of $u_j$ and $\delta_d$, $\delta_t$ have been reported in FS09 for the katabatic flow solution when compared to current DNS results, qualitatively resembling predictions of the analytic laminar flow solution.

Note that when the flow is forced through a constant surface buoyancy flux, as in the FS09 study, anabatic and katabatic flow solutions are constraint to share the same slope-normal integrated horizontal momentum flux $I_u^\alpha / I_u^{\alpha=90°} = 1/\sin\alpha$, hence the stronger variability of $\delta_d$ and $\delta_t$ in the FS09 katabatic flow solution, when compared to the current DNS results.

### 4.3. *TKE and buoyancy variance*

Slope-normal variations of TKE and of buoyancy variance $\langle b'b' \rangle$ are featured in figure 8. The buoyancy variance may also be interpreted as a form of turbulent potential energy. The stronger surface stable stratification that characterizes katabatic flows as the sloping angle decreases results in a weakening of TKE in the inner flow regions (below the LLJ), whereas the observed increase of TKE in the outer flow region as $\alpha$ decreases is likely related to the broadening of the flow length scales, which despite being modest for the katabatic flow solution, have an apparent effect on TKE. TKE profiles from the anabatic flow solution are again more sensitive to $\alpha$ when compared to their katabatic counterparts. In the anabatic flow cases, the peak TKE location increases as $\alpha$ decreases, but its magnitude shows non-monotonic behaviour, thus suggesting a more complex dependence on $\alpha$. Furthermore, the TKE in the neighbourhood of the LLJ is approximately constant throughout the considered flow regimes.

The buoyancy variance $\langle b'b' \rangle$ peaks in the near-wall regions for both flow regimes where strong buoyancy gradients occur, in agreement with findings from FS09. Variations in $\langle b'b' \rangle$ as a function of $\alpha$ in the below-LLJ region are significant only for the katabatic flow regime, with peak value and its location increasing and decreasing as $\alpha$ is reduced. The above-LLJ regions of the boundary layer are characterized by a rapid decay in $\langle b'b' \rangle$, most evident for the katabatic flow regime. The anisotropic nature of turbulence in slope flows is apparent from figure 9, where normal stress components $\langle u'u' \rangle$, $\langle v'v' \rangle$ and $\langle w'w' \rangle$ are compared. The boundary layer character of the system is apparent with the wall providing an effective damping of the $\langle w'w' \rangle$ central moment, in both anabatic and katabatic flow regimes. It is to be
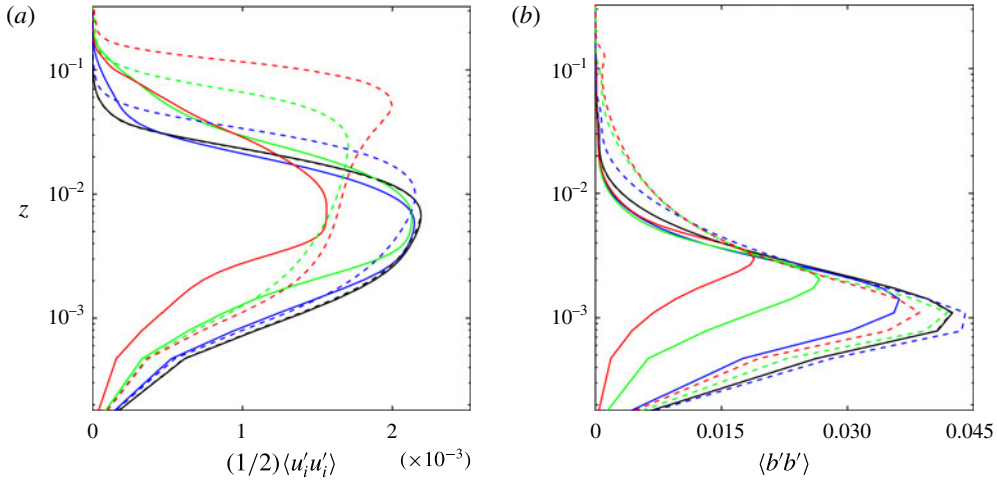
FIGURE 8. Comparison of turbulent kinetic energy $(1/2)\langle u_i' u_i' \rangle$ (*a*) and buoyancy variance ($\langle b'b' \rangle$) (*b*) for the katabatic (solid lines) and the anabatic flow (dashed lines) regimes at $\alpha = 90°$ (black), $\alpha = 60°$ (blue), $\alpha = 30°$ (green), and $\alpha = 15°$ (red). Simulations correspond to the highest $Gr = 2.1 \times 10^{11}$ cases. Recall that the $z$-axis denotes the slope-normal coordinate direction.
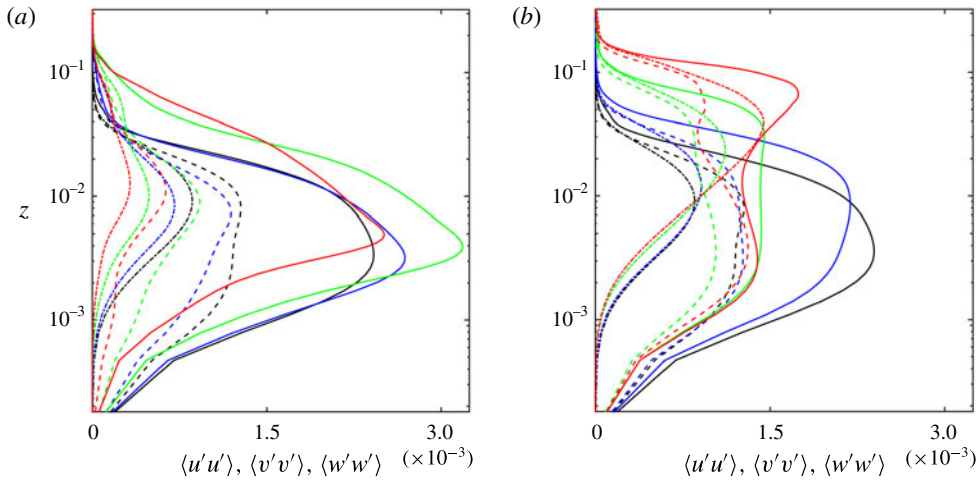


FIGURE 9. Normal stress components $\langle u'u' \rangle$ (solid lines), $\langle v'v' \rangle$ (dashed lines) and $\langle w'w' \rangle$ (dot-dashed lines) for the katabatic (*a*) and the anabatic (*b*) flow regimes at $\alpha = 90°$ (black), $\alpha = 60°$ (blue), $\alpha = 30°$ (green) and $\alpha = 15°$ (red). Simulations correspond to the highest $Gr = 2.1 \times 10^{11}$ cases (simulations S90H, S60H, S30H, and S15H and U90H, U60H, U30H and U15H, respectively).

noted the strong sensitivity of $\langle w'w' \rangle$ with respect to $\alpha$ for both wind regimes. This behaviour is related to the direct effect of stratification (background + perturbation) on $\langle w'w' \rangle$, given that buoyancy is effective at damping/exciting slope-normal velocity fluctuations $w'$. Because of this, as $\alpha$ decreases, the turbulence characterizing katabatic flows becomes more anisotropic (the strong, effective, stable stratification damps
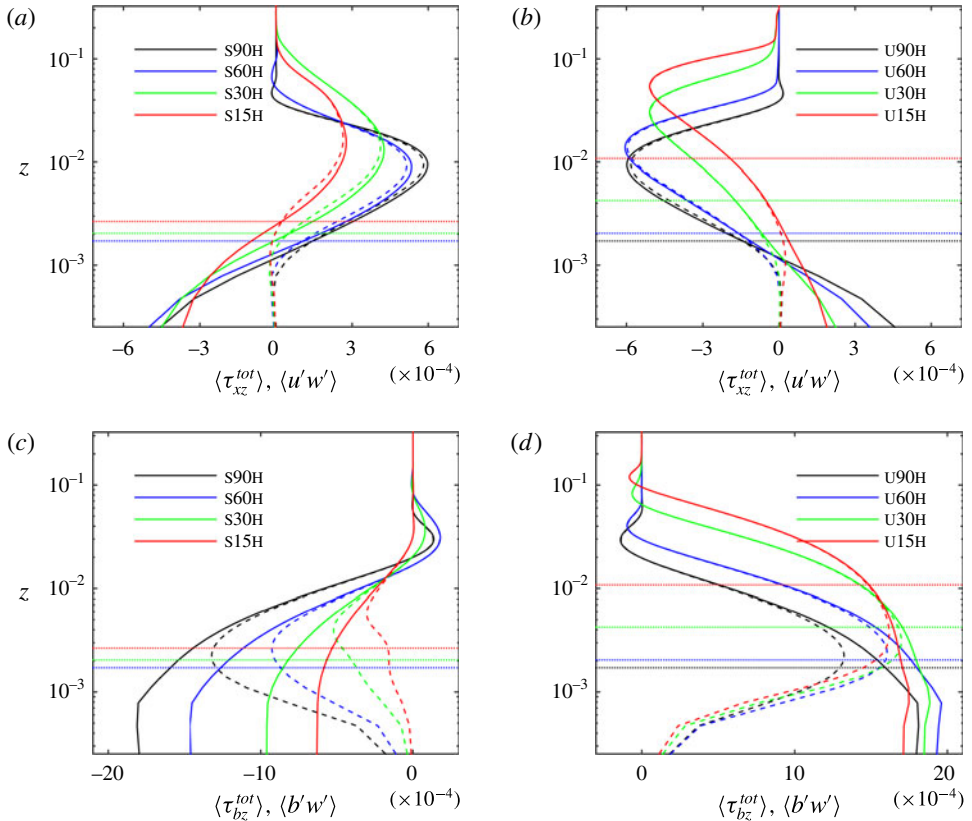
FIGURE 10. Total (solid lines) and turbulent (dashed lines) momentum flux for the katabatic (*a*) and the anabatic (*b*) flow regimes, and total (solid lines) and turbulent (dashed lines) buoyancy slope-normal flux for the katabatic (*c*) and the anabatic (*d*) flow regimes. All cases are characterized by $Gr = 2.1 \times 10^{11}$. $\langle \tau_{xz}^{tot} \rangle$ denotes the total slope-normal flux of momentum, whereas $\langle \tau_{bz}^{tot} \rangle$ denotes the total slope-normal buoyancy flux. The height of the LLJ ($z_j$) is displayed (horizontal lines) for the different cases to provide a reference.

$\langle w'w' \rangle$) in contrast to its anabatic counterpart, where the positive surface buoyancy leads to more isotropic turbulent motions. The observed trend here supports the recently proposed scaling of Shapiro & Fedorovich (2014) based on the assumption of large-scale separation between slope-normal and slope-parallel motions populating katabatic flows, which might indeed hold at small sloping angles.

### 4.4. *Momentum and buoyancy fluxes*

Turbulent and total (turbulent + molecular) vertical buoyancy and momentum fluxes are displayed in figure 10 for each of the considered runs. Turbulent buoyancy fluxes obey Fick's law of diffusion, whereas momentum fluxes consistently feature a thin layer just below the LLJ where counter gradient fluxes are observed. This feature is related to the extrema of the mean $\langle u \rangle$-profiles not being co-located with the zero crossing of the turbulent momentum fluxes. At the LLJ location for instance, a positive (negative) total slope-normal momentum flux for the katabatic (anabatic)
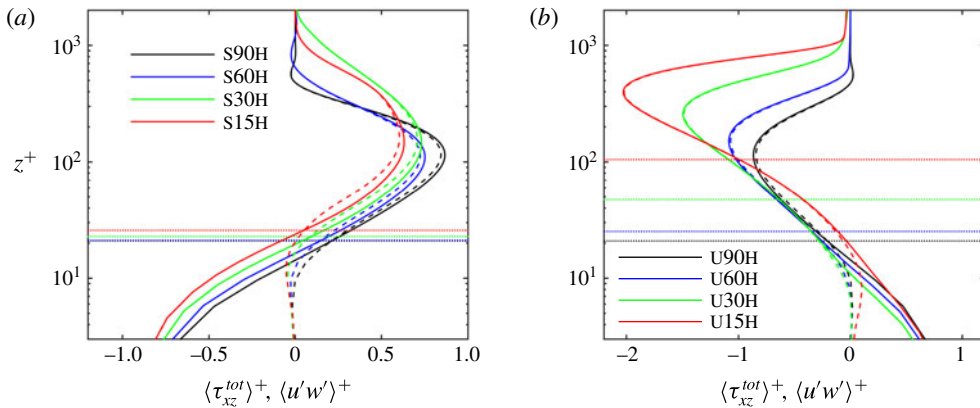
FIGURE 11. Total (solid lines) and turbulent (dashed lines) momentum flux for the katabatic (*a*) and the anabatic (*b*) flow regimes in inner units. All cases are characterized by $Gr = 2.1 \times 10^{11}$. $\langle \tau_{xz}^{tot} \rangle$ denotes the total slope-normal flux of momentum. The height of the LLJ ($z_j$) is displayed (horizontal lines) for the different cases to provide a reference.

flow regime are observed. Note that counter gradient fluxes have been previously reported in experimental studies (Smeets *et al.* 2000; Oldroyd *et al.* 2016*a*). The peak magnitude of both $\langle \tau_{xz}^{tot} \rangle$ and $\langle \tau_{bz}^{tot} \rangle$ in the above-LLJ regions is dependent on $\alpha$ for both flow regimes (it decreases as $\alpha$ decreases). In addition, katabatic flow solutions are characterized by a modest upward shift of flux extrema as the sloping angle decreases, whereas the upward shift is more significant for the anabatic flow cases. Such trends are directly related to the combined effects of $\alpha$ on the scales of the flow (recall that the analytic Prandtl solution predicts $L \propto (\sin(\alpha))^{-1/2}$) and of the surface induced stratification in katabatic and anabatic flows, whose strength increases as $\alpha$ decreases, progressively damping (for the katabatic cases) or enhancing (for the anabatic cases) turbulent fluctuations. In the FS09 study, the peak magnitude of $\langle \tau_{xz}^{tot} \rangle$ and $\langle \tau_{bz}^{tot} \rangle$ in the katabatic flow regime was found to be approximately constant and independent of $\alpha$. Conversely, it was sensitive to $\alpha$ in the anabatic flow cases, in apparent contrast with current findings. Such a mismatch is related to the different surface forcing approach that characterizes the current and the FS90 study (in FS90 a constant surface buoyancy flux is applied to drive the flow).

Figure 11 features the total and the turbulent momentum fluxes for the considered katabatic and anabatic flow regimes in inner units. For katabatic flows the viscous contribution to the total flux is dominant in the below-LLJ regions, and drops to less than 10 % as $z^+ > 50$ for the $\alpha = 90°$ case. As the sloping angle decreases the viscous contribution in the above-LLJ region increases, due to the strengthening of the stable stratification resulting from the imposed surface buoyancy, and amounts to approximately 35 % the total at $z^+ = 50$ for the shallower of the considered slopes ($\alpha = 15°$). In contrast, anabatic flows are characterized by a decrease of viscous contributions to the total momentum flux as the sloping angle decreases throughout the boundary layer, with viscous effects remaining dominant up to $z^+ \approx 12$, where viscous and turbulent fluxes are roughly of the same magnitude, and becoming negligible ($<10$ %) as $z^+ > 50$. From figure 11 is also apparent how the surface contribution in terms of total stress is larger than the peak stress in the above-LLJ region for katabatic flows, whereas for anabatic flows as the sloping angle decreases
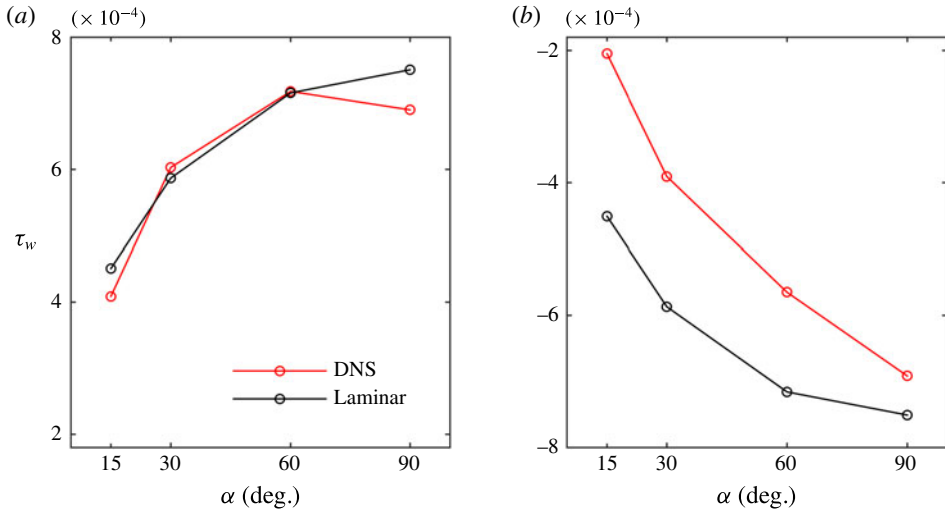
FIGURE 12. $\alpha$ dependence of the kinematic surface average stress $\tau_w$ for katabatic (*a*) and anabatic (*b*) flow cases. Simulations correspond to cases S90H, S60H, S30H, S15H and U90H, U60H, U30H, U15H for the katabatic and anabatic regimes, respectively. Predictions from the Prandtl laminar solution are included for comparison (black lines).

the surface stress becomes progressively smaller when compared to the outer stress peak.

Turbulent fluctuations contribute to the overall buoyancy flux in the below-LLJ region of katabatic flows, whereas they provide a negligible contribution to the overall momentum flux. This latter behaviour has direct effect on the overall surface stress, which is nearly equal to the laminar flow prediction for $\alpha > 90°$, as displayed in figure 12. Turbulent motion in the below-jet regions of katabatic flows are thus 'inactive' from a momentum transport perspective (in the Townsend (1956) sense), but are relatively effective in vertically transporting buoyancy. To the contrary, turbulent fluctuations in the anabatic flow solution contribute to both the overall surface buoyancy and momentum fluxes that progressively depart from their Prandtl 'laminar flow' counterparts as $\alpha$ is reduced. An interesting feature of the considered anabatic flow simulations is the magnitude of the time- and space-averaged surface total momentum flux ($\tau_w$), as displayed in figure 12. $\tau_w$ is consistently smaller than its laminar flow prediction in the anabatic cases, and its magnitude decreases as the sloping angle is reduced. Note that such feature might be related to the relatively modest $Gr$ value characterizing the various runs.

### 4.5. *The mean kinetic energy budget*

The governing equation for the time- and space-averaged velocity $\langle u_i \rangle$ is readily derived by applying Reynolds decomposition to the instantaneous flow variables (e.g. $u_i = \langle u_i \rangle + u'_i$) and space + time averaging (2.9). The budget equation for MKE is then obtained by multiplying the equation for $\langle u_i \rangle$ by $\langle u_i \rangle$ itself. Assuming horizontal homogeneity ($\partial \langle \cdot \rangle / \partial x = \partial \langle \cdot \rangle / \partial y = 0$) and no subsidence ($\langle w \rangle = 0$) it reads

$$\frac{\partial(\frac{1}{2}\langle u \rangle \langle u \rangle)}{\partial t} = \langle u'w' \rangle \frac{\partial \langle u \rangle}{\partial z} - \langle u \rangle \langle b \rangle \sin(\alpha) - \frac{\partial(\frac{1}{2}\langle u \rangle \langle u'w' \rangle)}{\partial z} + Gr^{-1/2}\langle u \rangle \frac{\partial^2 \langle u \rangle}{\partial z^2}, \quad (4.9)$$
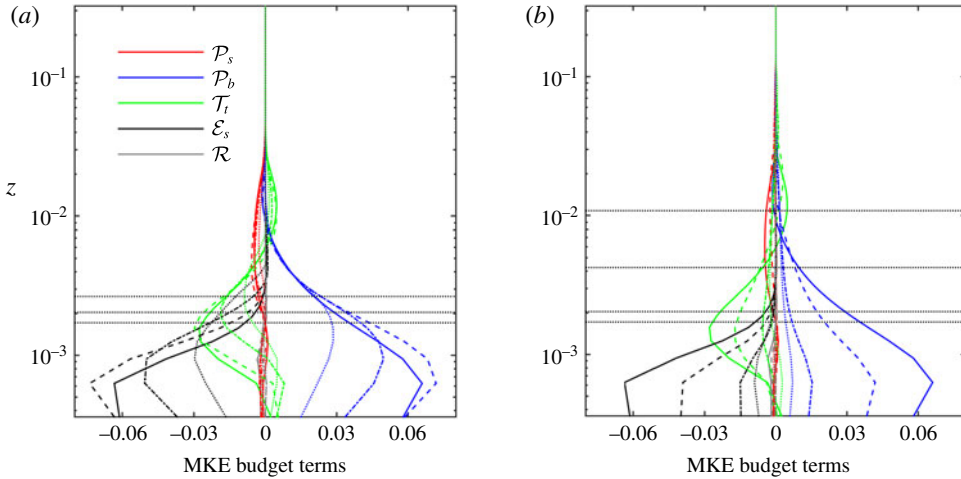
FIGURE 13. Slope-normal structure of the MKE budget for the katabatic (*a*) and for the anabatic (*b*) flow regimes at $\alpha = 90°$ (solid lines), $\alpha = 60°$ (dashed lines), $\alpha = 30°$ (dot-dashed lines) and $\alpha = 15°$ (dotted lines). All cases are characterized by $Gr = 2.1 \times 10^{11}$. The location of the LLJ is highlighted by horizontal lines for the various runs to provide a reference height (note that as $\alpha$ decreases the LLJ height increases). All terms are normalized by $\hat{U}^3 \hat{L}^{-1} \equiv \hat{b}_s^2 \hat{N}^{-1}$.

where the left-hand side of (4.9) is the storage term of MKE, $\mathcal{P}_s \equiv \langle u'w' \rangle (\partial \langle u \rangle / \partial z)$ denotes shear production/destruction of MKE, $\mathcal{P}_b \equiv -\langle u \rangle \langle b \rangle \sin(\alpha)$ denotes buoyancy production/destruction of MKE, transport of MKE by turbulent motions is $\mathcal{T}_t \equiv -\partial (1/2 \langle u \rangle \langle u'w' \rangle)/\partial z$ and dissipation of MKE by viscous diffusion is $\mathcal{E} \equiv Gr^{-1/2} \langle u \rangle (\partial^2 \langle u \rangle / \partial z^2)$. When time averaging over a sufficiently long time period then $\partial \langle \cdot \rangle / \partial t = 0$ and the storage term can be neglected.

The normalized MKE budget terms for the considered anabatic and katabatic runs are displayed in figure 13. The choice of $\hat{b}_s^2 \hat{N}^{-1}$ as a normalizing factor is not critical for the interpretation of the budget, since the relative magnitude of the terms is unchanged. As expected, the overall main source of MKE is from buoyancy production ($\mathcal{P}_b$), which peaks in the below-jet regions, and is characterized by a gradual decrease throughout the boundary layer. In the outer regions of the flow, $\mathcal{P}_b$ becomes a sink of MKE in both flow regimes starting from the zero crossing of $\langle b \rangle$ and up to the start of the return flow region. Here, energy is provided by turbulent transport ($\mathcal{T}_t$), which balances shear production ($\mathcal{P}_s$) and buoyant production ($\mathcal{P}_b$) (both $\mathcal{P}_s$ and $\mathcal{P}_b$ are a sink term of MKE in such layer). At the wall, buoyant production is overcome by dissipation for both upslope and downslope flows, and transport from turbulent motions is responsible to close the MKE budget. $\mathcal{T}_t$ acts as a sink of MKE in the highly energetic LLJ regions, displacing it toward the wall to balance the enhanced dissipation, and also into the outer layer of the flow.

In both anabatic and katabatic flow regimes, shear production of MKE ($\mathcal{P}_s$) acts as a sink of MKE in the above-jet regions, draining energy from the mean flow and transferring it to turbulence through the classical energy cascade process. Interestingly, for both regimes and all the considered sloping angles, the below-jet regions are characterized by $\mathcal{P}_s > 0$, highlighting a region of global energy backscatter, i.e. energy is transferred from the turbulent eddies to the mean flow. Forward scatter

is known to be mainly caused by vortex stretching by the mean strain rate, whereas backscatter indicates vortex compression by the mean strain rate, which is not commonly observed in canonical wall-bounded flows.

### 4.6. *The turbulent kinetic energy budget*

Under the assumptions leading to (4.9), the budget equation for TKE is given as

$$\frac{\partial \langle \frac{1}{2} u_i' u_i' \rangle}{\partial t} = -\langle u' w' \rangle \frac{\partial \langle u \rangle}{\partial z} + \langle b' w' \rangle \cos(\alpha) - \langle b' u' \rangle \sin(\alpha) - \frac{\partial \langle \frac{1}{2} u_i' u_i' w' \rangle}{\partial z}$$

$$- \frac{\partial \langle \pi' w' \rangle}{\partial z} + Gr^{-1/2} \frac{\partial^2 \langle \frac{1}{2} u_i' u_i' \rangle}{\partial z^2} - Gr^{-1/2} \left\langle \frac{\partial u_i'}{\partial x_j} \frac{\partial u_i'}{\partial x_j} \right\rangle, \qquad (4.10)$$

where $\partial \langle (1/2) u_i' u_i' \rangle / \partial t$ is the storage of TKE term, shear production of TKE is denoted as $P_s \equiv -\langle u' w' \rangle (\partial \langle u \rangle / \partial z)$, buoyant production/destruction of TKE is composed of two terms, namely $P_{b,1} \equiv \langle b' u' \rangle \sin(\alpha)$ and $P_{b,3} \equiv \langle b' w' \rangle \cos(\alpha)$, turbulent transport of TKE is $T_t \equiv -\partial \langle (1/2) u_i' u_i' w' \rangle / \partial z$, pressure transport $T_p \equiv -\partial \langle \pi' w' \rangle / \partial z$, viscous diffusion of TKE is $T_v \equiv Gr^{-1/2} \partial^2 \langle (1/2) u_i' u_i' \rangle / \partial z^2$ and viscous dissipation $\epsilon \equiv -Gr^{-1/2} \langle (\partial u_i' / \partial x_j)(\partial u_i' / \partial x_j) \rangle$. With regard to the buoyancy production/destruction terms, $P_{b,1}$ accounts for production/destruction of TKE due to cross-correlation between along-slope velocity ($u$) and buoyancy ($b$), whereas $P_{b,3}$ accounts for production/destruction of TKE due to cross-correlation between normal-to-slope velocity ($w$) and buoyancy ($b$). The splitting of the buoyancy production term is clearly a result of the inclined reference system that is adopted to describe the evolution of the system.

TKE budget terms for the considered runs (characterized by $Gr = 2.1 \times 10^{11}$) are displayed in figure 14. Shear production ($P_s$) appears with opposite signs in the budgets of MKE and TKE as expected. It represents the net transfer from MKE to TKE as the result of their interactions that often sustains turbulence in classical boundary layer theory on flat slopes. For both anabatic and katabatic flow regimes, $P_s$ is characterized by two positive peaks, one in the above jet regions and one in the very near-wall regions, and is negative in a small interval just below the LLJ, where global energy backscatter occurs. Occurrence of negative $P_s$ is related to the presence of local (in $z$) counter-gradient turbulent momentum flux, in line with findings of §4.4. In both katabatic and anabatic flow regimes, $\epsilon$ peaks at the wall, is approximately constant in the near-LLJ region and decreases logarithmically in the core of the flow. The $P_{b,3}$ is a sink of TKE for the katabatic regime and a source of TKE for the anabatic regime, as expected. In the anabatic regime $P_{b,3} = 0$ at $\alpha = 90°$, but gains considerable importance (as a TKE source term) in the overall budget as $\alpha$ decreases. For instance, considering the $\alpha = 15°$ run, $P_{b,3}$ alone overcomes TKE dissipation in the core of the LLJ. To the contrary, the modest magnitude of $P_{b,3}$ highlights how buoyant destruction of TKE is not the primary mechanism through which buoyancy acts to suppress turbulence in katabatic flows. Following the same reasoning of Shah & Bou-Zeid (2014) (where stability effects on the Ekman layer were studied through DNS), it is argued here that negative buoyancy directly reduces $\langle w' w' \rangle$, thus reducing local production of $\langle u' w' \rangle$. A reduction in $\langle u' w' \rangle$ would ultimately result in the observed decrease in $\langle P_s \rangle$ and related TKE magnitude as $\alpha$ decreases (i.e. as the static stability of the environment increases). $P_{b,1}$ is the major source of TKE at the LLJ for the katabatic flow regime at all the considered $\alpha$. On the other hand, in the anabatic flow regime $P_{b,3}$ overcomes $P_{b,1}$ as $\alpha$ decreases,
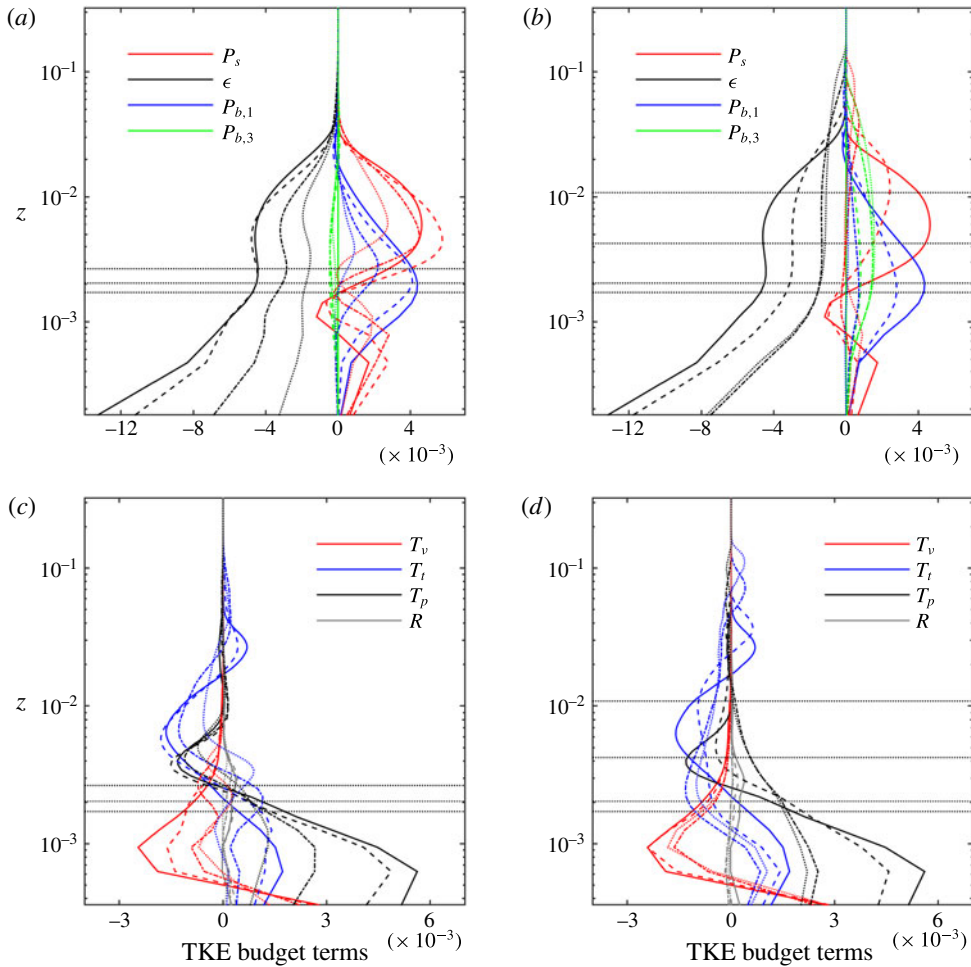
FIGURE 14. Comparison of TKE budged terms for katabatic ($a,c$) and anabatic ($b,d$) flow regimes at $\alpha = 90°$ (solid lines), $\alpha = 60°$ (dashed lines), $\alpha = 30°$ (dot-dashed lines) and $\alpha = 15°$ (dotted lines). All cases are characterized by $Gr = 2.1 \times 10^{11}$. Production and destruction terms ($a,b$) have been separated from transport and residual terms ($c,d$). The $z$-axis represents the slope-normal coordinate direction. The location of the LLJ is highlighted by horizontal lines for the various runs to facilitate interpretation (note that $\alpha \propto z_j$). All terms are normalized by $\hat{U}^3 \hat{L}^{-1} \equiv \hat{b}_s^2 \hat{N}^{-1}$.

becoming the leading buoyant production term. Overall, the sum of production terms ($P_s + P_{b,1} + P_{b,3}$) overcome dissipation in the above-jet regions (approximately up to $10z_j$), and transport terms are responsible for dislocating this excess in TKE down towards the wall and towards the outer regions of the flow. Turbulent transport ($T_t$) is a more effective carrier of TKE in the outer regions of the flow, whereas pressure fluctuations ($T_p$) are more effective in transporting TKE down toward the wall, to balance dissipation and viscous diffusion. The viscous diffusion term $T_v$ resembles its pressure-driven boundary layer analogue, where $T_v$ is a sink of TKE in the buffer sublayer, and a source of TKE in the laminar sublayer, below $z^+ = 5$ (corresponding to $z = 5 \times 10^{-4}$ in current units).
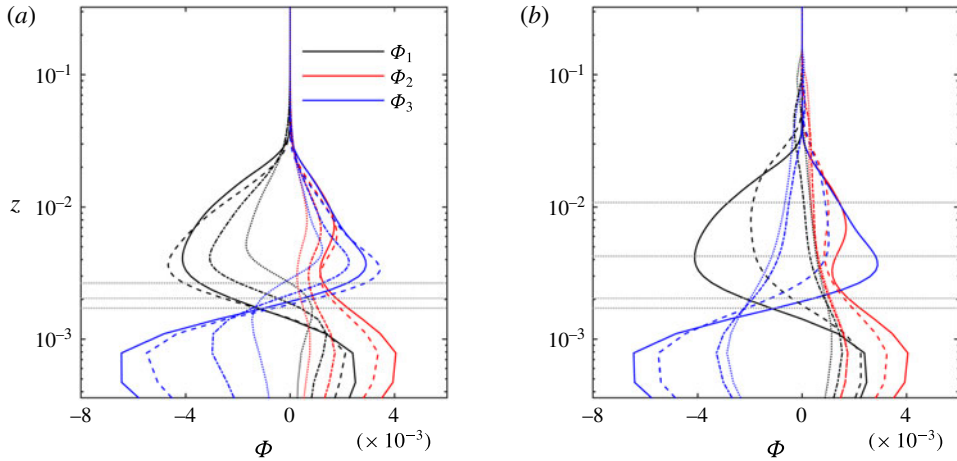
FIGURE 15. Comparison of return-to-isotropy terms for katabatic (*a*) and anabatic (*b*) flow regimes at $Gr = 2.1 \times 10^{11}$. We denote $\Phi_1 \equiv \langle p'(\partial u'/\partial x) \rangle$, $\Phi_2 \equiv \langle p'(\partial v'/\partial y) \rangle$ and $\Phi_3 \equiv \langle p'(\partial w'/\partial z) \rangle$. The location of the LLJ is once again highlighted with horizontal lines and the $\alpha = 90°$, $60°$, $30°$ and $15°$ runs (simulations S90H, S60H, S30H, S15H for the katabatic regimes; U90H, U60H, U30H, U15H for the anabatic regimes) are denoted with solid, dashed, dot-dashed and dotted lines respectively. The *z*-axis represents the slope-normal coordinate direction and all terms are normalized by $\hat{U}^3 \hat{L}^{-1} \equiv \hat{b}_s^2 \hat{N}^{-1}$.

Not shown here is the vertical structure of flux Richardson number ($Ri_f = \langle b'w' \rangle / (\mathrm{d}\langle u \rangle / \mathrm{d}z) \langle u'w' \rangle$), which is positive (negative) throughout the core of the boundary layer (above the LLJ and below the return flow region) in the katabatic (anabatic) flow regimes. In the katabatic flow regime $Ri_f$ is lower in magnitude than its critical value of 0.25, except in the neighbourhood of the LLJ the stable stratification and low velocity gradients result instead in $Ri_f \gg 1$.

It is worth noting the significant contribution of turbulent and pressure transport terms in the neighbourhood of the LLJ and in the wall regions in both flow regimes. Pressure fluctuations are relevant in the near-wall regions when compared to corresponding values observed in neutral (Moser, Kim & Moin 1999) and stably stratified (Iida, Kasagi & Nagano 2002) pressure-driven channel flow DNS. In the neighbourhood of the LLJ $Ri_f$ is relatively large in magnitude (not shown) for both flow regimes, promoting strong internal gravity wave activity, which does not transfer buoyancy, but can be effective in transporting momentum through the action of pressure force, thus justifying such relevant contribution of pressure transport to the TKE budget.

The return-to-isotropy term (also known as pressure redistribution term) contracts to zero, and so vanishes from the TKE budget equation (4.10). However, when analysed for the single TKE budget components displayed in figure 15, the role of turbulence in distributing turbulent energy becomes clear. For instance, wall damping effects on slope-normal velocity fluctuations are apparent in the below-LLJ regions, where $\Phi_3 < 0$ indicating energy redistribution from the slope-normal component ($\langle w'w' \rangle$) to the horizontal components ($\langle u'u' \rangle$ and $\langle v'v' \rangle$ respectively). In the above-jet regions for the katabatic flow regime, a consistent energy redistribution among the TKE components are observed across the sloping angles with energy being transferred from the streamwise component ($\langle u'u' \rangle$) to the spanwise and slope-normal components

($\langle v'v' \rangle$ and $\langle w'w' \rangle$ respectively). For the anabatic flow regime, the return-to-isotropy terms in the above-jet regions highlight a transition in the system as a function of $\alpha$. When the two highest sloping angles are considered ($\alpha = 60°$ and $\alpha = 90°$), energy transfer is qualitatively equivalent to that characterizing the katabatic flow regime, i.e. the streamwise variance feeds the spanwise and slope-normal variance components. For $\alpha = 15°$ and $\alpha = 30°$, the return-to-isotropy term becomes a sink for $\langle w'w' \rangle$ and a source for $\langle u'u' \rangle$ and $\langle v'v' \rangle$, indicative of energy transfer from the slope-normal TKE component to the streamwise and spanwise TKE components. This transition suggests that at low sloping angles, anabatic flow regimes are characterized by slope-normal elongated eddies as apparent from figure 5, which feed $\langle u'u' \rangle$ and $\langle v'v' \rangle$ from $\langle w'w' \rangle$, the latter being directly sustained by the slope-normal projection of the buoyancy force $b \cos(\alpha)$. Conversely, katabatic flow eddies are streamwise elongated and remove energy from $\langle u'u' \rangle$ – directly fed by the streamwise component of the buoyancy force – to transfer it to $\langle w'w' \rangle$ and $\langle v'v' \rangle$. This energy redistribution term ensures some self-preservation of the slope-normal velocity variance in katabatic flows despite the adverse role of stability.

Overall, the proposed TKE budget analysis suggests a subdivision of the boundary layer into four distinct regions, for the considered $\alpha$- and $Gr$-ranges, namely

(i) an outer layer, corresponding approximately to the return flow region, where turbulent transport ($T_t$) is the main source of TKE and balances dissipation ($\epsilon$);

(ii) an intermediate layer, bounded below by the LLJ and capped above by the outer layer, where the sum of shear and buoyant production ($P_s + P_{b,1} + P_{b,3}$) overcomes dissipation ($\epsilon$), and where turbulent and pressure transport terms ($T_t$, $T_p$) are a sink of TKE;

(iii) a buffer layer, corresponding to $5 \lesssim z^+ \lesssim 30$, where TKE is provided by turbulent and pressure transport terms, to balance viscous diffusion and dissipation;

(iv) a laminar sublayer, corresponding to $z^+ \lesssim 5$, where the influence of viscosity is significant and the flow is approximately laminar.

## 5. Summary and conclusions

DNS are used to characterize mean flow and turbulence of thermally driven flows along a uniformly cooled or heated sloping plate immersed within a stably stratified environment, using a set-up resembling the one considered by Prandtl's slope-flow model. The study focused on sensitivity of the flow statistics to variations in the sloping angle ($\alpha$) and Grashof number ($Gr$) for a fixed molecular Prandtl number ($Pr = 1$). Four sloping angles ($\alpha = 15°$, $30°$, $60°$ and $90°$) and three Grashof number ($Gr = 5 \times 10^{10}$, $Gr = 1 \times 10^{11}$, and $Gr = 2.1 \times 10^{11}$) were considered, where $Gr = \hat{b}_s^4 \hat{\nu}^{-2} \hat{N}^{-6}$ is interpreted as the ratio between the energy production at the surface and the work against the background stratification and viscous forces. The study complements the Fedorovich & Shapiro (2009) analysis, where a similar range of sloping angle and $Gr$ was considered but where the flow was forced using a constant surface buoyancy flux.

The initial transient is characterized by slowly decaying quasi-stationary oscillatory patterns in the spatially integrated variables, the normalized oscillation frequency being proportional to the sine of the sloping angle, in agreement with field observations of slope flows (e.g. Princevac *et al.* 2008; Monti *et al.* 2014) and with findings from a recent theoretical work (Fedorovich & Shapiro 2017). The quality of the averaging operation has been tested against a dynamic and an energy identity derived from the
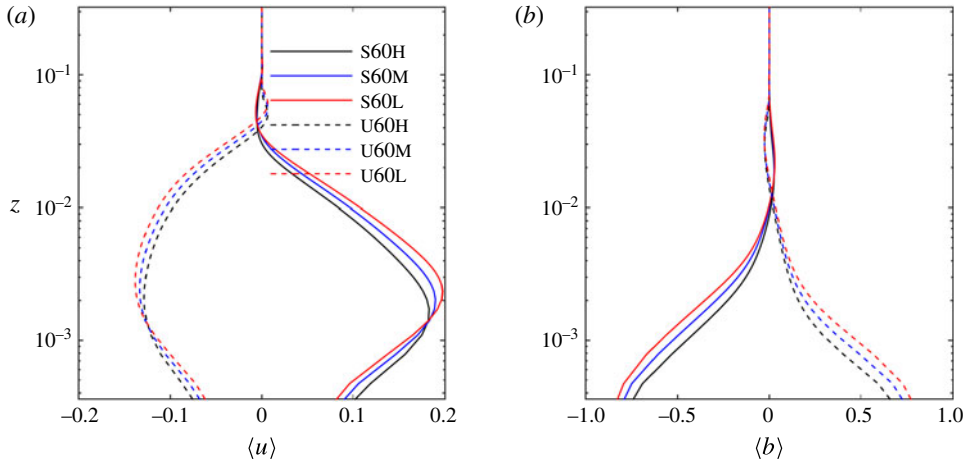
FIGURE 16. Sensitivity of the streamwise velocity $\langle u \rangle$ (a) and buoyancy $\langle b \rangle$ (b) on the *Gr* parameter, for katabatic (solid lines) and anabatic (dashed lines) flow regimes at $\alpha = 60°$.

equations of motions, that the time-averaged solution must satisfy in coordinates of statistical homogeneity.

With respect to their basic features, the katabatic and anabatic mean flow appear similar to their corresponding laminar (Prandtl) counterparts. The thermal boundary layer is much shallower when compared to the dynamic boundary layer, the latter being characterized by a low-level jet near the wall regions, and by a weak return flow in the outer regions. Turbulent anabatic and katabatic regimes are found to be structurally similar at high sloping angles but to undergo a different transition in the turbulence production and transport mechanisms as the sloping angle decreases. In fact, a stark statistical difference between the two flow regimes for the $\alpha \lessapprox 30°$ range was noted from the DNS analysis. As $\alpha$ decreases, the negative surface buoyancy driving downslope flows leads to the formation of a strong surface inversion layer, resulting in a progressive laminarization of the solution in the near-LLJ regions. It also results in small variation in the integrated horizontal momentum flux and in an overall small variability of mean profiles with respect to $\alpha$. Anabatic flows on the other hand are characterized by a strengthening of TKE production and turbulent momentum fluxes as $\alpha$ decreases, by a significant $\alpha$ dependence of the overall horizontal momentum flux, and by well mixed profiles of buoyancy and velocity, suggesting the presence of convective cells for $\alpha \lessapprox 30°$. Analysis of the slope-normal integrated energy equation highlights how the characteristic (normalized) scale of anabatic flow $\mathcal{L} \propto 1/\sin \alpha$, whereas the characteristic scale of katabatic flow is found to be poorly sensitive to $\alpha$. As in Fedorovich & Shapiro (2009), no region with constancy (even approximate) of any of the fluxes with distance from the wall has been identified, and molecular diffusion of momentum and buoyancy are found to be significant in the below-LLJ regions, when compared to turbulent diffusion. Budget equations show how MKE is fed into the fluid system through the imposed surface buoyancy, and turbulent fluctuations redistribute it from the lower edge of the jet toward the wall and toward the outer layer. Interestingly, as *Gr* increases, the overall normalized energy of the system is reduced, but turbulent fluctuations gain importance in the below-jet regions. Hence, despite the modest Grashof number range considered here, one might speculate about the existence of a (turbulent) overlap layer at higher
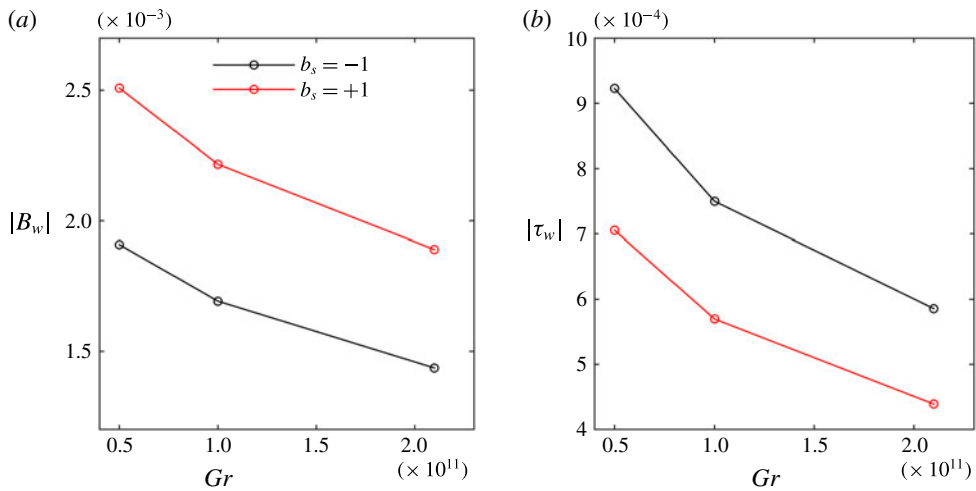
FIGURE 17. Absolute value of the averaged surface buoyancy flux (*a*) and momentum flux (*b*) as a function of *Gr* for anabatic (red line) and katabatic (black line) flow regimes at $\alpha = 60°$ (simulations S60H, S60M, S60L and U60H, U60M, U60L, respectively).

*Gr*, located in the below-jet region, separating the LLJ from the laminar sublayer. In addition, a zone of global backscatter (energy transfer from the turbulent eddies to the mean flow) is consistently found just below the LLJ, which highlights the presence of vortex compression (instead of stretching) dynamical mechanisms, and failure of gradient diffusion theory in such layer. The behaviour in returning to isotropy of turbulent fluctuations further highlights how katabatic and anabatic flow systems differ in their mechanisms sustaining turbulence at shallow slopes, and again indicates presence of convective cells for $\alpha \lesssim 30°$ in anabatic flows. Overall, analysis of the $\alpha$ dependence of the TKE budget terms suggests a subdivision of the boundary layer in four distinct regions: (i) an outer layer, approximately corresponding to the return flow region, where turbulent transport balances dissipation, (ii) an intermediate layer, bounded below by the LLJ, where shear and buoyant production overcome dissipation, and turbulent and pressure fluctuations are responsible to relocate the excess TKE down toward the wall and toward the outer layer, (iii) a buffer layer, capped above by the LLJ, where pressure and turbulent transport balance dissipation and viscous diffusion of TKE and (iv) a laminar sublayer, where molecular viscosity and thermal diffusivity effects are of leading order in the transport of momentum and buoyancy.

The proposed DNS results, in particular the TKE and MKE budgets, and the role of turbulence isotropization via pressure fluctuations can be used to guide improvements in current turbulence closure modelling for sloping and stable conditions that can then be implemented in the next generation of large-scale atmospheric models.

## Appendix A. Sensitivity of solutions to variations in the Grashof number

### A.1. *Mean flow, TKE and buoyancy variance*

The sensitivity of mean velocity and buoyancy profiles to variations in *Gr* is displayed in figure 16 for anabatic and katabatic flow regimes characterized by $\alpha = 60°$. Increases in *Gr* results in weaker thermal and dynamic boundary layers, i.e. in a
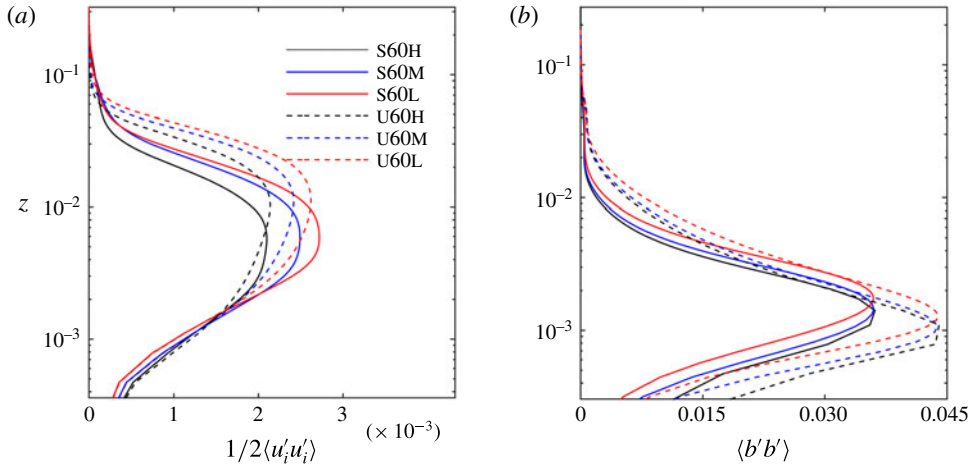
FIGURE 18. Sensitivity of the turbulent kinetic energy $((1/2)\langle u_i' u_i' \rangle)$ (*a*) and buoyancy variance $(\langle b' b' \rangle)$ (*b*) to the *Gr* parameter for katabatic (solid lines) and anabatic (dashed lines) flow regimes at $\alpha = 60°$.
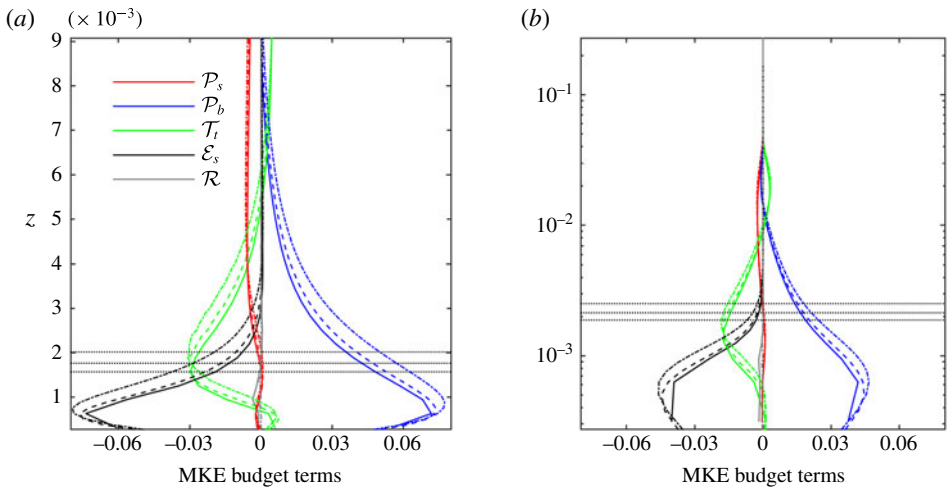


FIGURE 19. Sensitivity of MKE budget terms to *Gr* for the katabatic (*a*) and the anabatic (*b*) flow regimes at $\alpha = 60°$. Profiles correspond to $Gr = 1 \times 10^{10}$ (dot-dashed lines), $Gr = 5 \times 10^{11}$ (dashed lines) and $Gr = 2.1 \times 10^{11}$ (solid lines). The location of the LLJ is highlighted with horizontal dotted black lines for the various runs, to provide a reference height (note that as *Gr* increases the LLJ height decreases). All terms are normalized by $\hat{U}^3 \hat{L}^{-1} \equiv \hat{b}_s^2 \hat{N}^{-1}$.

decrease of $z_j$, $u_j$, $\delta$, as well as $\int_0^H \langle b \rangle \, dz$ and $\int_0^H \langle u \rangle \, dz$. As apparent from figure 17, increases in *Gr* results in a decrease in the surface buoyancy flux $\langle \tau_{bz} \rangle|_{z=0}$, i.e. in a reduction of the rate of potential energy that is supplied to the system, as could have been intuitively predicted. Surface momentum fluxes are also decreasing as *Gr* increases, as also displayed in figure 17. Conversely, the magnitude of slope-normal surface gradients of along-slope velocity and buoyancy are stronger as *Gr* increases,
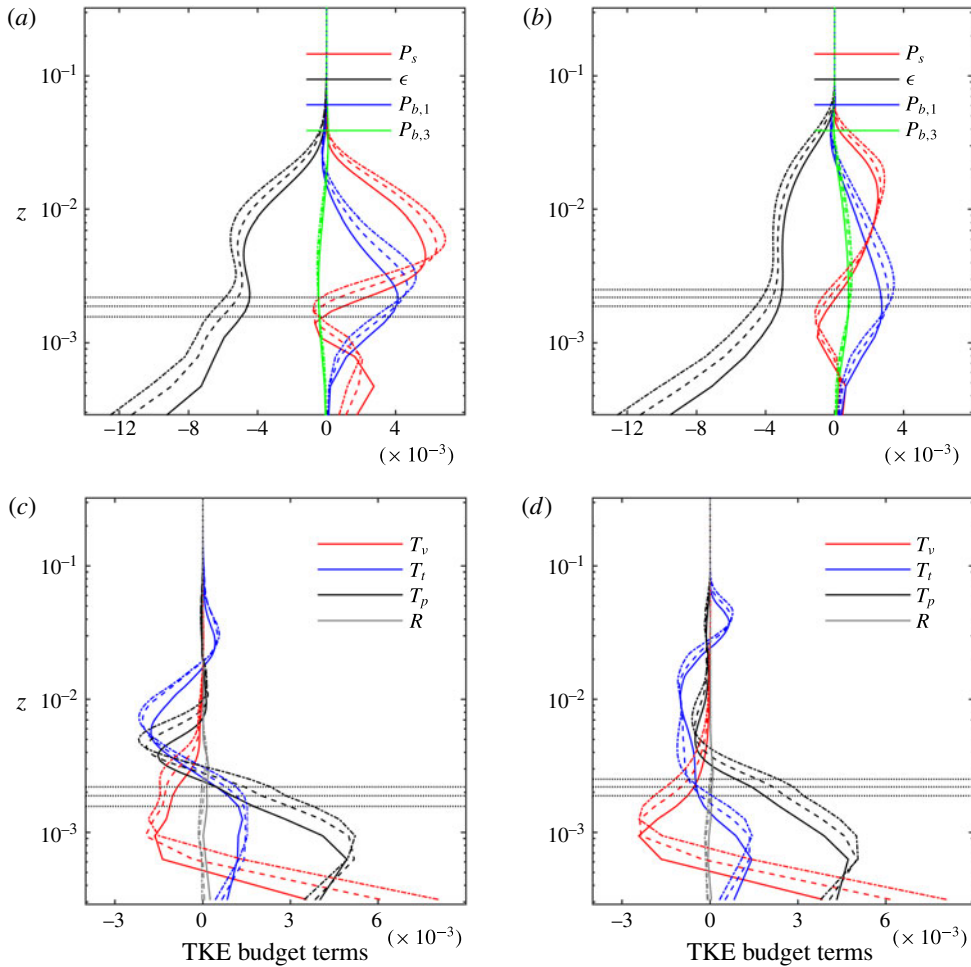
FIGURE 20. Sensitivity of TKE budget terms to $Gr$ for the katabatic ($a,c$) and the anabatic ($b,d$) flow regimes at $\alpha = 60°$. Profiles correspond to $Gr = 5 \times 10^{10}$ (dot-dashed lines), $Gr = 1 \times 10^{11}$ (dashed lines), and $Gr = 2.1 \times 10^{11}$ (solid lines). The $z$-axis represents the slope-normal coordinate direction. The location of the LLJ is highlighted with dotted black lines for the various runs, to provide a reference height (note that as $Gr$ increases the LLJ height decreases). All terms are normalized by $\hat{U}^3 \hat{L}^{-1} \equiv \hat{b}_s^2 \hat{N}^{-1}$.

highlighting a relatively stronger momentum (buoyancy) replenishment (extraction) induced by turbulent fluctuations. Therefore as $Gr$ increases, the LLJ becomes weaker but better mixed.

The relatively stronger role of turbulent fluctuations in the near-wall regions as $Gr$ increases is apparent if one focuses on figure 18, where TKE and buoyancy variance are featured for both flow regimes. Higher $Gr$ results in stronger near-wall TKE and $\langle b'b' \rangle$, despite the relatively lower kinetic and potential energy of the system, when compared to the same simulation at lower $Gr$. Worth noting also how the near-surface peak of $\langle b'b' \rangle$ is insensitive to $Gr$. This behaviour is in line with findings from mean profiles, which suggest a stronger role of turbulent fluctuations in the near-wall region as $Gr$ increases. In the above-LLJ regions TKE, $\langle b'b' \rangle$ and the slope-normal scale of

the flow increase in magnitude as *Gr* is reduced for all the considered cases, likely due to the relatively stronger dynamic and thermal boundary layers.

## A.2. *MKE and TKE budget terms*

The dependence of MKE budget terms on *Gr* is highlighted in figure 19. Besides the expected decrease in the slope-normal scale as *Gr* increases, one of the main features of the MKE budget terms is a relative strengthening of $\mathcal{P}_s$ and $\mathcal{T}_t$ in the below-LLJ regions as *Gr* increases. With this regard, note how the peak value of $\mathcal{P}_b$ and $\epsilon_s$ are sensitive to variations in *Gr*, whereas the peak value of $\mathcal{P}_s$ and $\mathcal{T}_t$ are insensitive to *Gr*.

As *Gr* increases, TKE budget terms are characterized by a strengthening of $P_s$ in the neighbourhood of the LLJ and near-surface regions for the katabatic flow regimes (see figure 20). Anabatic flows are instead characterized by a strengthening of $P_s$ in the near-wall regions, well below $z_j$. In addition, buoyant production $P_{b,1}$ increases as *Gr* increases in the below LLJ regions and transport terms tend to decrease. This suggests that at higher *Gr* when compared to those considered herein, anabatic and katabatic flows might be characterized by a relatively important local TKE production rate in the below-LLJ regions, and negligible TKE transport rates, ultimately resulting in stronger TKE, and thus larger $z_j$ and well-mixed profiles of buoyancy and velocity. Such a region might well be the equivalent of the overlap (logarithmic) layer in canonical wall-bounded turbulent flows, which is not observed here, probably because of the relatively low *Gr* values.

## REFERENCES

ABKAR, M., BAE, H. J. & MOIN, P. 2016 Minimum-dissipation scalar transport model for large-eddy simulation of turbulent flows. *Phys. Rev. Fluids* **1** (4), 041701.

ALBERTSON, J. D. & PARLANGE, M. B. 1999*a* Natural integration of scalar fluxes from complex terrain. *Adv. Water Resour.* **23** (3), 239–252.

ALBERTSON, J. D. & PARLANGE, M. B. 1999*b* Surface length scales and shear stress: implications for land-atmosphere interaction over complex terrain. *Water Resour. Res.* **35** (7), 2121–2132.

ARDUINI, G., STAQUET, C. & CHEMEL, C. 2016 Interactions between the nighttime valley-wind system and a developing cold-air pool. *Boundary-Layer Meteorol* **161** (1), 49–72.

AXELSEN, S. & DOP, H. 2009*a* Large-eddy simulation of katabatic winds. Part 1: comparison with observations. *Acta Geophys.* **57** (4), 803–836.

AXELSEN, S. L. & DOP, H. 2009*b* Large-eddy simulation of katabatic winds. Part 2: sensitivity study and comparison with analytical models. *Acta Geophys.* **57** (4), 837–856.

BOU-ZEID, E., MENEVEAU, C. & PARLANGE, M. B. 2005 A scale-dependent Lagrangian dynamic model for large eddy simulation of complex turbulent flows. *Phys. Fluids* **17** (2), 025105.

BOU-ZEID, E., OVERNEY, J., ROGERS, B. D. & PARLANGE, M. B. 2009 The effects of building representation and clustering in large-eddy simulations of flows in urban canopies. *Boundary-Layer Meteorol.* **132** (3), 415–436.

BURKHOLDER, B., FEDOROVICH, E. & SHAPIRO, A. 2011 Evaluating subgrid-scale models for large-eddy simulation of turbulent katabatic flow. In *Qual Reliab Large-eddy Simulations II*, pp. 149–160. Springer.

BURKHOLDER, B., SHAPIRO, A. & FEDOROVICH, E. 2009 Katabatic flow induced by a cross-slope band of surface cooling. *Acta Geophys.* **57** (4), 923–949.

BURNS, P. & CHEMEL, C. 2014 Evolution of cold-air-pooling processes in complex terrain. *Boundary-Layer Meteorol.* **150** (3), 423–447.

BURNS, P. & CHEMEL, C. 2015 Interactions between downslope flows and a developing cold-air pool. *Boundary-Layer Meteorol.* **154** (1), 57–80.

CALAF, M., MENEVEAU, C. & MEYERS, J. 2010 Large eddy simulation study of fully developed wind-turbine array boundary layers. *Phys. Fluids* **22** (1), 015110.

CALAF, M., PARLANGE, M. B. & MENEVEAU, C. 2011 Large eddy simulation study of scalar transport in fully developed wind-turbine array boundary layers. *Phys. Fluids* **23** (12), 126603.

CANUTO, C., HUSSAINI, M. Y., QUARTERONI, A. & ZANG, T. A. 2006 *Spectral Methods*. Springer.

CHAMECKI, M., MENEVEAU, C. & PARLANGE, M. B. 2009 Large eddy simulation of pollen transport in the atmospheric boundary layer. *J. Aero. Sci.* **40**, 241–255.

CHEMEL, C., STAQUET, C. & LARGERON, Y. 2009 Generation of internal gravity waves by a katabatic wind in an idealized alpine valley. *Meteorol. Atmos. Phys.* **103** (1–4), 187–194.

CHORIN, A. J. 1968 Numerical solution of the Navier–Stokes equations. *Math. Comput.* **22** (104), 745–762.

CHOW, F. K., WEIGEL, A. P., STREET, R. L., ROTACH, M. W. & XUE, M. 2006 High-resolution large-eddy simulations of flow in a steep Alpine valley. Part I: Methodology, verification, and sensitivity experiments. *J. Appl. Meteorol. Climatol.* **45** (1), 63–86.

CHU, P. C. 1987 An instability theory of ice-air interaction for the formation of ice edge bands. *J. Geophys. Res.* **92** (C7), 6966–6970.

DEFANT, F. 1949 Zur theorie der hangwinde, nebst bemerkungen zur theorie der berg- und talwinde. *Arch. Meteorol. Geophys. Bioklimatol. Ser* A **1**, 421–450.

DENBY, B. 1999 Second-order modelling of turbulence in katabatic flows. *Boundary-Layer Meteorol.* **92** (1), 65–98.

DORAN, J. C. & HORST, T. W. 1981 Velocity and temperature oscillations in drainage winds. *J. Appl. Meteorol.* **20** (4), 361–364.

EGGER, J. 1985 Slope winds and the axisymmetric circulation over Antarctica. *J. Atmos. Sci.* **42** (17), 1859–1867.

FEDOROVICH, E. & SHAPIRO, A. 2009 Structure of numerically simulated katabatic and anabatic flows along steep slopes. *Acta Geophys.* **57** (4), 981–1010.

FEDOROVICH, E. & SHAPIRO, A. 2017 Oscillations in Prandtl slope flow started from rest. *Q. J. R. Meteorol. Soc.* **143** (703), 670–677.

FERNANDO, H. J. S. 2010 Fluid dynamics of urban atmospheres in complex terrain. *Annu. Rev. Fluid Mech.* **42** (1), 365–389.

FERNANDO, H. J. S., PARDYJAK, E. R, DI SABATINO, S., CHOW, F. K., DE WEKKER, S. F., HOCH, S. W., HACKER, J., PACE, J. C., PRATT, T., PU, Z. *et al.* 2015 The MATERHORN: Unraveling the intricacies of mountain weather. *Bull. Am. Meteorol. Soc.* **96** (11), 1945–1967.

GIOMETTO, M. G., CHRISTEN, A., MENEVEAU, C., FANG, J., KRAFCZYK, M. & PARLANGE, M. B. 2016 Spatial characteristics of roughness sublayer mean flow and turbulence over a realistic urban surface. *Boundary-Layer Meteorol.* **160** (3), 425–452.

GIOMETTO, M. G., GRANDI, R., FANG, J., MONKEWITZ, P. A. & PARLANGE, M. B. 2017 Katabatic flow: a closed-form solution with spatially-varying eddy diffusivities. *Boundary-Layer Meteorol* **162** (2), 307–317.

GRACHEV, A. A., LEO, L. S., SABATINO, S. D., FERNANDO, H. J. S., PARDYJAK, E. R. & FAIRALL, C. W. 2016 Structure of turbulence in katabatic flows below and above the wind-speed maximum. *Boundary-Layer Meteorol.* **159** (3), 469–494.

GREUELL, J. W., BROEKE VAN DEN, M. R., KNAP, W., REIJMER, C., SMEETS, P. & STRUIJK, I. 1994 PASTEX: a glacio-meteorological experiment on the Pasterze (Austria). *Tech. Rep.*, Institute for Marine and Atmospheric Research, University, Utrecht.

GRISOGONO, B. & AXELSEN, S. L. 2012 A note on the pure katabatic wind maximum over gentle slopes. *Boundary-Layer Meteorol.* **145** (3), 527–538.

GRISOGONO, B., JURLINA, T., VEČENAJ, Ž. & GÜTTLER, I. 2014 Weakly nonlinear Prandtl model for simple slope flows. *Q. J. R. Meteorol. Soc.* **141**, 883–892.

GRISOGONO, B., KRALJEVIC, L. & JERICEVIC, A. 2007 The low-level katabatic jet height versus Monin Obukhov height. *Q. J. R. Meteorol. Soc.* **133**, 2133–2136.

GRISOGONO, B. & OERLEMANS, J. 2001a A theory for the estimation of surface fluxes in simple katabatic flows. *Q. J. R. Meteorol. Soc.* **127**, 2725–2739.

GRISOGONO, B & OERLEMANS, J 2001b Katabatic flow: analytic solution for gradually varying eddy diffusivities. *J. Atmos. Sci.* **58** (21), 3349–3354.

GRISOGONO, B. & OERLEMANS, J. 2002 Justifying the WKB approximation in pure katabatic flows. *Tellus* **54** (5), 453–462.

GUTMAN, L. N. 1983 On the theory of the katabatic slope wind. *Tellus* **35A**, 213–218.

GÜTTLER, I., MARINOVIĆ, I., VEČENAJ, Ž & GRISOGONO, B. 2016 Energetics of slope flows: linear and weakly nonlinear solutions of the extended Prandtl model. *Front. Earth Sci.* **4** (July), 1–13.

HAIDEN, T. & WHITEMAN, C. D. 2005 Katabatic flow mechanisms on a low-angle slope. *J. Appl. Meteorol.* **44** (1), 113–126.

HANG, C., NADEAU, D. F., GULTEPE, I., HOCH, S. W., ROMÁN-CASCÓN, C., PRYOR, K., FERNANDO, H. J. S., CREEGAN, E. D., LEO, L. S. & SILVER, Z. 2016 A case study of the mechanisms modulating the evolution of valley fog. *Pure Appl. Geophys.* **173** (9), 1–20.

HIGGINS, C. W., PARLANGE, M. B. & MENEVEAU, C. 2003 Alignment trends of velocity gradients and subgrid-scale fluxes in the turbulent atmospheric boundary layer. *Boundary-Layer Meteorol.* **109** (1), 59–83.

HULTMARK, M., CALAF, M. & PARLANGE, M. B. 2013 A new wall shear stress model for atmospheric boundary layer simulations. *J. Atmos. Sci.* **70** (11), 3460–3470.

IIDA, O., KASAGI, N. & NAGANO, Y. 2002 Direct numerical simulation of turbulent channel flow under stable density stratification. *Intl J. Heat Mass Transfer* **45**, 1693–1703.

ISRAELI, M. & ORSZAG, S. A. 1981 Approximation of radiation boundary conditions. *J. Comput. Phys.* **41** (1), 115–135.

JENSEN, D. D., NADEAU, D. F., HOCH, S. W. & PARDYJAK, E. R. 2016 Observations of near-surface heat-flux and temperature profiles through the early evening transition over contrasting surfaces. *Boundary-Layer Meteorol.* **159** (3), 567–587.

KAVAVCIC, I. & GRISOGONO, B. 2007 Katabatic flow with Coriolis effect and gradually varying eddy diffusivity. *Boundary-Layer Meteorol.* **125** (2), 377–387.

KRAVCHENKO, A. G. G. & MOIN, P. 1997 On the effect of numerical errors in large eddy simulations of turbulent flows. *J. Comput. Phys.* **131** (2), 310–322.

KUMAR, V., KLEISSL, J., MENEVEAU, C. & PARLANGE, M. B. 2006 Large-eddy simulation of a diurnal cycle of theatmospheric boundary layer: atmospheric stabilityand scaling issues. *Water Resour. Res.* **42**, W06D09.

LEHNER, M., WHITEMAN, C. D., HOCH, S. W., JENSEN, D., PARDYJAK, E. R., LEO, L. S., DI SABATINO, S. & FERNANDO, H. J. S. 2015 A case study of the nocturnal boundary layer evolution on a slope at the foot of a desert mountain. *J. Appl. Meteorol. Climatol.* **54** (4), 732–751.

LU, H. & PORTÉ-AGEL, F. 2010 A modulated gradient model for large-eddy simulation: application to a neutral atmospheric boundary layer. *Phys. Fluids* **22** (1), 015109.

MAHRT, L. 1982 Momentum balance of gravity flows. *J. Atmos. Sci.* **39** (12), 2701–2711.

MAHRT, L. 1998 Stratified atmospheric boundary layers and breakdown of models. *Theor. Comput. Fluid Dyn.* **11**, 263–279.

MAHRT, L. 2013 Stably stratified atmospheric boundary layers. *Annu. Rev. Fluid Mech.* **46** (July), 23–45.

MCNIDER, R. T. 1982 A note on velocity fluctuations in drainage flows. *J. Atmos. Sci.* **39** (7), 1658–1660.

MENOLD, E. R. & YANG, K. 1962 Asymptotic solutions for unsteady laminar free convection on a vertical plate. *J. Appl. Mech.* **29** (1), 124–126.

MONTI, P., FERNANDO, H. J. S. & PRINCEVAC, M. 2014 Waves and turbulence in katabatic winds. *Environ. Fluid Mech.* **14** (2), 431–450.

MONTI, P., FERNANDO, H. J. S., PRINCEVAC, M., CHAN, W. C., KOWALEWSKI, T. A. & PARDYJAK, E. R. 2002 Observations of flow and turbulence in the nocturnal boundary layer over a slope. *J. Atmos. Sci.* **59** (17), 2513–2534.

MOSER, R. D., KIM, J. & MOIN, P. 1999 Direct numerical simulation of turbulent channel flow up to *Re* = 590. *Phys. Fluids* **11** (4), 11–13.

NADEAU, D. F., PARDYJAK, E. R., HIGGINS, C. W., HUWALD, H. & PARLANGE, M. B. 2013*a* Flow during the evening transition over steep Alpine slopes. *Q. J. R. Meteorol. Soc.* **139** (672), 607–624.

NADEAU, D. F., PARDYJAK, E. R., HIGGINS, C. W. & PARLANGE, M. B. 2013*b* Similarity scaling over a steep alpine slope. *Boundary-Layer Meteorol.* **147** (3), 401–419.

OERLEMANS, J. 1998 The atmospheric boundary layer over melting glaciers. In *Clear Cloudy Bound Layers*, pp. 129–153. Royal Netherlands Academy of Arts and Sciences.

OERLEMANS, J., BJÖRNSSON, H., KUHN, M., OBLEITNER, F., PALSSON, F., SMEETS, C. J. P. P., VUGTS, H. F. & WOLDE, J. D. 1999 Glacio-meteorological investigation on Vatnajokull, Iceland, summer 1996: an overview. *Boundary-Layer Meteorol.* **92** (1), 3–24.

OLDROYD, H. J., KATUL, G. G., PARDYJAK, E. R. & PARLANGE, M. B. 2014 Momentum balance of katabatic flow on steep slopes covered with short vegetation. *Geophys. Res. Lett.* **41** (13), 4761–4768.

OLDROYD, H. J., PARDYJAK, E. R., HIGGINS, C. W. & PARLANGE, M. B. 2016*a* Buoyant turbulent kinetic energy production in steep-slope katabatic flow. *Boundary-Layer Meteorol.* **161** (3), 405–416.

OLDROYD, H. J., PARDYJAK, E. R., HUWALD, H. & PARLANGE, M. B. 2016*b* Adapting tilt corrections and the governing flow equations for steep, fully three-dimensional, mountainous terrain. *Boundary-Layer Meteorol.* **159** (3), 539–565.

ORSZAG, S. A. 1969 Numerical methods for the simulation of turbulence. *Phys. Fluids* **12** (12), II–250.

ORSZAG, S. A. 1970 Transform method for the calculation of vector-coupled sums: application to the spectral form of the vorticity equation. *J. Atmos. Sci.* **27** (6), 890–895.

ORSZAG, S. A. & PAO, Y. H. 1975 Numerical computation of turbulent shear flows. In *Advances in Geophysics*, vol. 18, pp. 225–236. Elsevier.

PARISH, T. R. 1992 On the role of Antarctic katabatic winds in forcing large-scale tropospheric motions. *J. Atmos. Sci.* **49** (15), 1374–1385.

PARISH, T. R. & BROMWICH, D. H. 1998 A case study of Antarctic katabatic wind interaction with large-scale forcing. *Mon. Weath. Rev.* **126** (1), 199–209.

PARMHED, O., OERLEMANS, J. & GRISOGONO, B. 2004 Describing surface fluxes in katabatic flow on Breidamerkurjo kull, Iceland. *Q. J. R. Meteorol. Soc.* **130**, 1137–1151.

POPE, S. B. 2000 *Turbulent Flows*. Cambridge University Press.

PORTÉ-AGEL, F., MENEVEAU, C. & PARLANGE, M. B. 2000 A scale-dependent dynamic model for large-eddy simulation: application to a neutral atmospheric boundary layer. *J. Fluid Mech.* **415**, 261–284.

PRANDTL, L. 1942 *Führer durch die Strömungslehre*. Vieweg & Sohn.

PRINCEVAC, M., HUNT, J. C. R. & FERNANDO, H. J. S. 2008 Quasi-steady katabatic winds on slopes in wide valleys: hydraulic theory and observations. *J. Atmos. Sci.* **65** (2), 627–643.

RAMPANELLI, G., ZARDI, D. & ROTUNNO, R. 2004 Mechanisms of up-valley winds. *J. Atmos. Sci.* **61** (24), 3097–3111.

RENFREW, I. A. 2004 The dynamics of idealized katabatic flow over a moderate slope and ice shelf. *Q. J. R. Meteorol. Soc.* **130** (598), 1023–1045.

RENFREW, I. A. & ANDERSON, P. S. 2006 Profiles of katabatic flow in summer and winter over Coats Land, Antarctica. *Q. J. R. Meteorol. Soc.* **132** (616), 779–802.

ROTACH, M. W. & ZARDI, D. 2007 On the boundary-layer structure over highly complex terrain: Key findings from MAP. *Q. J. R. Meteorol. Soc.* **133** (625), 937–948.

SCHUMANN, U. 1990 Large-eddy simulation of the up-slope boundary layer. *Q. J. R. Meteorol. Soc.* **116** (493), 637–670.

SHAH, S. K. & BOU-ZEID, E. 2014 Direct numerical simulations of turbulent Ekman layers with increasing static stability: modifications to the bulk structure and second-order statistics. *J. Fluid Mech.* **760**, 494–539.

SHAPIRO, A. & FEDOROVICH, E. 2004 Prandtl number dependence of unsteady natural convection along a vertical plate in a stably stratified fluid. *Intl J. Heat Mass Transfer* **47** (22), 4911–4927.

SHAPIRO, A. & FEDOROVICH, E. 2005 Natural convection in a stably stratified fluid along vertical plates and cylinders with temporally periodic surface temperature variations. *J. Fluid Mech.* **546**, 295–311.

SHAPIRO, A. & FEDOROVICH, E. 2007 Katabatic flow along a differentially cooled sloping surface. *J. Fluid Mech.* **571**, 149–175.

SHAPIRO, A. & FEDOROVICH, E. 2008 Coriolis effects in homogeneous and inhomogeneous katabatic flows. *Q. J. R. Meteorol. Soc.* **134** (631), 353–370.

SHAPIRO, A. & FEDOROVICH, E. 2014 A boundary-layer scaling for turbulent katabatic flow. *Boundary-Layer Meteorol.* **153** (1), 1–17.

SHARMA, V., CALAF, M., LEHNING, M. & PARLANGE, M. B. 2016 Time-adaptive wind turbine model for an LES framework. *Wind Energy* **19** (5), 939–952.

SHARMA, V., PARLANGE, M. B. & CALAF, M. 2017 Perturbations to the spatial and temporal characteristics of the diurnally-varying atmospheric boundary layer due to an extensive wind farm. *Boundary-Layer Meteorol.* **162** (2), 255–282.

SKYLLINGSTAD, E. D. 2003 Large-eddy simulation of katabatic flows. *Boundary-Layer Meteorol.* **106** (2), 217–243.

SMEETS, C. J. P. P., DUYNKERKE, P. G. & VUGTS, H. F. 1997 Turbulence characteristics of the stable boundary layer over a mid-latitude glacier. Part 1: a combination of katabatic and large-scale forcing. *Boundary-Layer Meteorol.* **87**, 117–145.

SMEETS, C. J. P. P., DUYNKERKE, P. G. & VUGTS, H. F. 2000 Turbulence characteristics of the stable boundary layer over a mid-latitude glacier. Part 2: pure katabatic forcing conditions. *Boundary-Layer Meteorol.* **97**, 73–107.

SMITH, C. M. & SKYLLINGSTAD, E. D. 2005 Numerical simulation of katabatic flow with changing slope angle. *Mon. Weath. Rev.* **133** (11), 3065–3080.

TEMAM, R. 1968 Une methode d'approximation de la solution des equations de Navier–Stokes. *Bull. Soc. Maths France* **96**, 115–152.

TOWNSEND, A. A. 1956 *The Structure of Turbulent Shear Flow*. Cambridge University Press.

WEIGEL, A. P., CHOW, F. K., ROTACH, M. W., STREET, R. L. & XUE, M. 2006 High-resolution large-eddy simulations of flow in a steep alpine valley. Part II: flow structure and heat budgets. *J. Appl. Meteorol. Climatol.* **45** (1), 87–107.

WHITEMAN, C. D. 1990 Observations of thermally developed wind systems in mountainous terrain. *Atmos Process over complex terrain, Meteor. Monogr.* **23** (45), 5–42.

ZARDI, D. & SERAFIN, S. 2015 An analytic solution for time-periodic thermally driven slope flows. *Q. J. R. Meteorol. Soc.* **141**, 1968–1974.

ZARDI, D. & WHITEMAN, C. D. 2013 Diurnal mountain wind systems. In *Mt Weather Res Forecast*, pp. 35–119. Springer.